UNIVERSITY OF AMSTERDAM

UvA-DARE (Digital Academic Repository)

Impact of neutrino flavor oscillations on the neutrino-driven wind nucleosynthesis of an electron-capture supernova

Pllumbi, E.; Tamborra, I.; Wanajo, S.; Janka, H.-T.; Hüdepohl, L.

DOI
10.1088/0004-637X/808/2/188

Publication date
2015

Document Version
Final published version

Published in
Astrophysical Journal

Link to publication

Citation for published version (APA):
Pllumbi, E., Tamborra, I., Wanajo, S., Janka, H-T., & Hüdepohl, L. (2015). Impact of neutrino flavor oscillations on the neutrino-driven wind nucleosynthesis of an electron-capture supernova. *Astrophysical Journal*, *808*(2), [188]. https://doi.org/10.1088/0004-637X/808/2/188

General rights
It is not permitted to download or to forward/distribute the text or part of it without the consent of the author(s) and/or copyright holder(s), other than for strictly personal, individual use, unless the work is under an open content license (like Creative Commons).

Disclaimer/Complaints regulations
If you believe that digital publication of certain material infringes any of your rights or (privacy) interests, please let the Library know, stating your reasons. In case of a legitimate complaint, the Library will make the material inaccessible and/or remove it from the website. Please Ask the Library: https://uba.uva.nl/en/contact, or a letter to: Library of the University of Amsterdam, Secretariat, Singel 425, 1012 WP Amsterdam, The Netherlands. You will be contacted as soon as possible.

UvA-DARE is a service provided by the library of the University of Amsterdam (https://dare.uva.nl)

Download date:23 Aug 2022

The Astrophysical Journal, 808:188 (19pp), 2015 August 1 doi:10.1088/0004-637X/808/2/188
© 2015. The American Astronomical Society. All rights reserved.

IMPACT OF NEUTRINO FLAVOR OSCILLATIONS ON THE NEUTRINO-DRIVEN WIND NUCLEOSYNTHESIS OF AN ELECTRON-CAPTURE SUPERNOVA

Else Pllumbi[1,2], Irene Tamborra[3], Shinya Wanajo[4], Hans-Thomas Janka[1], and Lorenz Hüdepohl[1]
[1] Max-Planck-Institut für Astrophysik, Karl-Schwarzschild-Str. 1, D-85748 Garching, Germany;
epllumbi@mpa-garching.mpg.de, thj@mpa-garching.mpg.de, lorenz@mpa-garching.mpg.de
[2] Physik Department, Technische Universität München, James-Franck-Straße 1, D-85748 Garching, Germany
[3] GRAPPA Institute, University of Amsterdam, Science Park 904, 1098 XH Amsterdam, The Netherlands; i.tamborra@uva.nl
[4] iTHES Research Group, RIKEN, Wako, Saitama 351-0198, Japan; shinya.wanajo@riken.jp
Received 2014 June 10; accepted 2015 May 25; published 2015 August 4

ABSTRACT

Neutrino oscillations, especially to light sterile states, can affect nucleosynthesis yields because of their possible feedback effect on the electron fraction (Y_e). For the first time, we perform nucleosynthesis calculations for neutrino-driven wind trajectories from the neutrino-cooling phase of an 8.8 $M_\odot$ electron-capture supernova (SN), whose hydrodynamic evolution was computed in spherical symmetry with sophisticated neutrino transport and whose Y_e evolution was post-processed by including neutrino oscillations between both active and active–sterile flavors. We also take into account the α-effect as well as weak magnetism and recoil corrections in the neutrino absorption and emission processes. We observe effects on the Y_e evolution that depend in a subtle way on the relative radial positions of the sterile Mikheyev–Smirnov–Wolfenstein resonances, on collective flavor transformations, and on the formation of α particles. For the adopted SN progenitor, we find that neutrino oscillations, also to a sterile state with eV mass, do not significantly affect the element formation and in particular cannot make the post-explosion wind outflow neutron-rich enough to activate a strong *r*-process. Our conclusions become even more robust when, in order to mimic equation-of-state-dependent corrections due to nucleon potential effects in the dense-medium neutrino opacities, six cases with reduced Y_e in the wind are considered. In these cases, despite the conversion of active neutrinos to sterile neutrinos, Y_e increases or is not significantly lowered compared to the values obtained without oscillations and active flavor transformations. This is a consequence of a complicated interplay between sterile-neutrino production, neutrino–neutrino interactions, and α-effect.

Key words: neutrinos – nuclear reactions, nucleosynthesis, abundances – supernovae: general

1. INTRODUCTION

Stars with mass larger than $\sim 8\,M_\odot$ end their life as core-collapse supernovae (CCSNe; e.g., Woosley et al. 2002). In particular, those with initial mass between ~ 8 and $\sim 10\,M_\odot$ form an electron-degenerate core composed of oxygen, neon, and magnesium (O–Ne–Mg) and end their life either as O–Ne–Mg white dwarfs or as "electron-capture supernovae" (ECSNe; Nomoto 1987), when electrons are captured on Ne and Mg triggering the collapse of the stellar core. Since ECSNe represent up to 30% of all CCSNe (Ishimaru & Wanajo 1999; Poelarends et al. 2008; Wanajo et al. 2011b), they could significantly contribute to the Galactic chemical enrichment with heavy elements (Ishimaru & Wanajo 1999).

ECSNe were suggested as candidate sites for the *r*-process (rapid neutron-capture) element production (Hillebrandt et al. 1984; Wanajo et al. 2003; Ning et al. 2007). For comprehensive reviews on the *r*-process, see Wanajo & Ishimaru (2006), Arnould et al. (2007), and Thielemann et al. (2011). However, recent nucleosynthesis studies (Hoffman et al. 2008; Wanajo et al. 2009), based on self-consistent hydrodynamic simulations of the explosion (Kitaura et al. 2006; Janka et al. 2008), do not support the production of elements with mass number heavier than $A \sim 110$ in the early ejecta of ECSNe, but suggest interesting production of light trans-iron elements from Zn to Zr (Wanajo et al. 2011b), of ^{48}Ca (Wanajo et al. 2013a), and of ^{60}Fe (Wanajo et al. 2013b). Two-dimensional hydrodynamic simulations do not provide conditions for a strong *r*-process. However, a weak *r*-process cannot be excluded, if the ejecta were slightly more neutron-rich than obtained in the models.

After the launch of the SN explosion, the proto-neutron star (PNS) cools because of the neutrino emission. Due to capture reactions and scattering events, neutrinos deposit energy in the outer layers of the PNS, giving birth to an outflow mainly composed of free neutrons and protons, the so-called neutrino-driven (ν-driven) wind—see Janka (2012) and Arcones & Thielemann (2013) for recent reviews on the topic. While expanding away from the neutron star, the ν-driven wind matter cools and nucleons recombine, producing alpha particles and some fraction of heavy nuclei. The ν-driven wind has long been considered as a promising site of the *r*-process (Meyer et al. 1992; Takahashi et al. 1994; Woosley et al. 1994; Qian & Woosley 1996; Otsuki et al. 2000; Wanajo et al. 2001; Thompson et al. 2001). However, the outcome of the ν-driven wind nucleosynthesis is strongly sensitive to the electron fraction Y_e (number of protons per nucleon), the entropy and the expansion timescale. Recent long-time hydrodynamic SN simulations with elaborate neutrino transport (Fischer et al. 2010; Hüdepohl et al. 2010) show, besides insufficient entropy, a trend toward proton-rich ν-driven winds, rather than neutron-rich ones as would be required for an *r*-process to occur. Such proton-rich conditions might be suitable for the νp-process making some light *p*-nuclei (Fröhlich et al. 2006a, 2006b; Pruet et al. 2006; Wanajo 2006).

More recently, however, it has been pointed out that the mean-field shift of nucleon potential energies (Reddy et al. 1998) significantly alters the charged-current neutrino opacity in the neutrinospheric layer and reduces Y_e from

initially proton-rich values down to possibly ∼0.42–0.45 for some temporary phase of the wind evolution (Martínez-Pinedo et al. 2012; Roberts 2012; Roberts et al. 2012). This effect was not adequately included in previous simulations, and it becomes important only when the neutrinosphere reaches high densities (postbounce time $t_{\rm pb} >$ a few hundred ms). At very late times, however, high neutrinospheric densities suppress ν_e absorption on neutrons by final-state Pauli blocking of electrons (Fischer et al. 2012), ν_e escape with harder spectra, and Y_e in the wind increases again. The matter at early and probably late times is thus still expected to be proton-rich.

One has to wonder whether favorable conditions for the *r*-process could still occur in SNe. Since Y_e depends on the competition between the capture rates of ν_e and $\bar{\nu}_e$ on free nucleons and their inverse reactions (Fuller & Meyer 1995), a modification of the predicted neutrino energy spectra, for example due to nucleon-potential effects, could affect Y_e in the neutrino-driven outflows. Moreover, neutrino flavor oscillations could modify the wind-Y_e, if they significantly alter the ν_e and $\bar{\nu}_e$ fluxes before Y_e reaches its asymptotic value. Therefore, the inclusion of flavor oscillations may be crucial for determining the nuclear production in the ν-driven wind matter and to clarify whether ECSNe could still be considered as candidate sites for the *r*-process.

The nucleosynthesis yields (and the *r*-process) in SNe might be affected by the existence of light sterile neutrinos, hypothetical gauge-singlet fermions that could mix with one or more of the active states and thus show up in active–sterile flavor oscillations (see Abazajian et al. 2012; Palazzo 2013 for recent reviews on the topic). In particular, eV-mass sterile neutrinos with large mixing imply that the ν_e flux would undergo Mikheyev–Smirnov–Wolfenstein (MSW) conversions (Mikheyev & Smirnov 1985; Wolfenstein 1978) to ν_s closer to the SN core than any other oscillation effect. We assume that the sterile state is heavier than the active ones because of cosmological neutrino mass limits (Abazajian et al. 2012). The idea that removing the ν_e flux by active–sterile oscillations could favor a neutron-rich outflow environment was proposed some time ago (Nunokawa et al. 1997; McLaughlin et al. 1999; Fetter 2000; Fetter et al. 2003; Beun et al. 2006; Hidaka & Fuller 2007; Keränen et al. 2007). However, the considered mass differences were larger and the possible impact of ν–ν interactions in the active sector (Duan et al. 2010) was not taken into account.

Recently, low-mass sterile neutrinos have been invoked to explain the excess $\bar{\nu}_e$ events in the LSND experiment (Aguilar et al. 2001; Strumia 2002; Gonzalez-Garcia & Maltoni 2008) as well as the MiniBooNE excess (Aguilar-Arevalo et al. 2009a, 2009b; Karagiorgi et al. 2009; MiniBooNE Collaboration et al. 2013). Moreover an indication for the possible existence of eV-mass sterile neutrinos comes from a new analysis of reactor $\bar{\nu}_e$ spectra and short-baseline experiments (Giunti & Laveder 2011a, 2011b; Kopp et al. 2011, 2013; Donini et al. 2012; Giunti et al. 2012, 2013). The cosmic microwave background anisotropies (Hamann et al. 2010; Reid et al. 2010; Archidiacono et al. 2013; Hinshaw et al. 2013; Hou et al. 2013; Planck Collaboration et al. 2013) point toward a cosmic excess radiation compatible with one family of fully thermalized sub-eV sterile neutrinos or one or even two partially thermalized sterile neutrino families with sub-eV/eV mass (Archidiacono et al. 2013, 2014; Giusarma et al. 2014).

Such intense activity triggered new interest in the role of neutrino oscillations with and without sterile neutrinos, and including ν–ν interactions, in nucleosynthesis processes like the *r*-process and the νp-process in SN outflows (Duan et al. 2011a; Martínez-Pinedo et al. 2011; Tamborra et al. 2012b; Wu et al. 2015).

The role of active–sterile neutrino mixing in the ν-driven explosion mechanism and the nucleosynthesis in the early ($t \leqslant 100$ ms postbounce) ejecta of ECSNe was discussed by Wu et al. (2014). The authors found that active–sterile conversions can not only suppress neutrino heating considerably but also potentially enhance the neutron-richness of the ejecta, allowing for the production of the elements from Sr, Y, and Zr up to Cd. The conclusiveness of these results is unclear, however, because, besides approximate modeling of neutrino oscillations, only spherically symmetric models were considered, although multi-dimensional effects had been shown to be important during the onset of the explosion (cf. Wanajo et al. 2011b). In contrast to spherical models, multi-dimensional ones provide sufficient neutron excess to yield interesting amounts of elements between the Fe-group and $N = 50$ nuclei even without involving sterile neutrino effects (Wanajo et al. 2011b).

In this work, we explore the impact of neutrino flavor oscillations (with and without the inclusion of an extra eV-mass sterile neutrino) on the Y_e evolution of the ν-driven wind and on the corresponding nucleosynthesis yields of an ECSN, whose evolution can be well described in spherical symmetry and has been followed beyond the explosion continuously into the subsequent PNS cooling phase (Hüdepohl et al. 2010). The simulation of Hüdepohl et al. (2010) did not include the aforementioned nucleon mean-field effects in the charged-current neutrino–nucleon reactions and resulted in the ejection of proton-rich matter throughout the wind phase. We still use this model to examine neutrino oscillation effects in the neutrino-driven wind, because the wind dynamics and thermodynamics conditions are only marginally changed despite the impact of the nucleon potentials on the electron fraction (e.g., Martínez-Pinedo et al. 2012).

Our paper is structured in the following way. In Section 2, we describe the ν-driven wind trajectories adopted for the nucleosynthesis calculations, as well as our reaction network. In Section 3, the electron fraction evolution and the nucleosynthesis results are presented when no neutrino oscillations occur as the fiducial case. After introducing the neutrino mass-mixing parameters in Section 4, we briefly discuss the oscillation physics involved in the nucleosynthesis calculations in Section 5. Our results for Y_e and how it is affected by neutrino oscillations (with and without sterile neutrinos) including the corresponding nucleosynthesis are presented in Section 6. In Section 7, we introduce six toy model cases for the ν_e and $\bar{\nu}_e$ energy spectra in order to explore the possible consequences of nuclear mean-field effects in the neutrino opacities. In Section 8, we discuss our results and compare with other works. We present our conclusions and perspectives in Section 9. In the Appendix, we give more details about the feedback of neutrino self-interactions on Y_e.

2. NEUTRINO-DRIVEN WIND AND REACTION NETWORK

We use one-dimensional (1D) long-time simulations of a representative 8.8 $M_\odot$ progenitor (Hüdepohl et al. 2010),

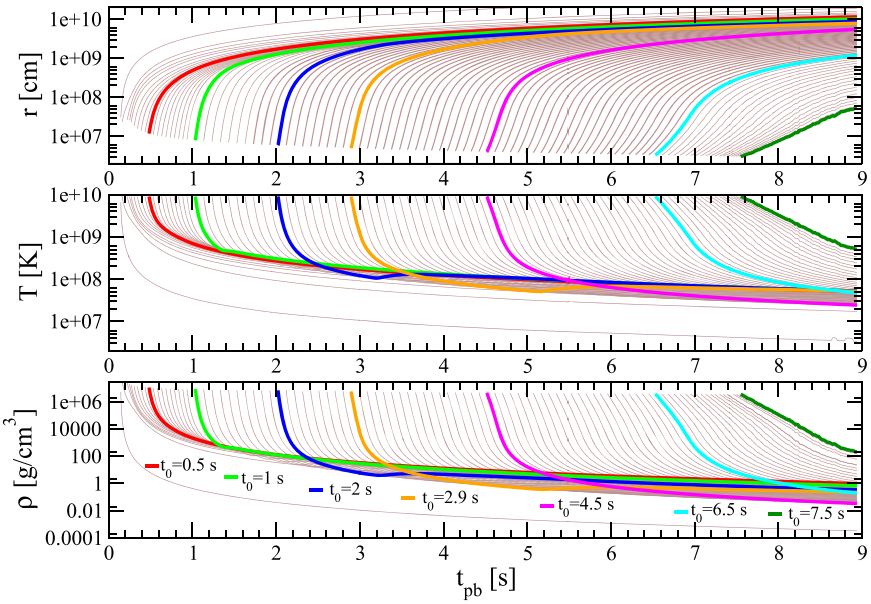

Figure 1. Mass-shell trajectories of the neutrino-driven wind as functions of postbounce time ($t_{\rm pb}$): radial distance from the PNS center (top), temperature (middle), and density (bottom) along the ejecta trajectories. The colored curves correspond to the selected seven trajectories representative of the evolution of the ν-driven wind at initial times $t_0 = 0.5$, 1, 2, 2.9, 4.5, 6.5, 7.5 s. The kinks visible in the temperature and density evolutions of the trajectories at $t_0 = 2$ and 2.9 s indicate the existence of a weak reverse shock.

performed with the equation of state of Shen et al. (1998). For the present study we adopt the Model Sf 21 (see Hüdepohl et al. 2010 for further details).[5] In the chosen model, the accretion phase ends already at a postbounce time of $t_{\rm pb} \sim 0.2$ s when neutrino heating drives the expansion of the postshock layers and powers the explosion. The subsequent deleptonization and cooling of the PNS were followed for ∼10 s.

In order to perform the network calculations for the nucleosynthesis in the neutrino-driven wind, we use 98 ejecta trajectories. Figure 1 shows the time evolution of the distance r from the center of the PNS (top panel), temperature T (middle panel), and matter density ρ (bottom panel) for these mass-shell trajectories as functions of $t_{\rm pb}$. The outflow evolution of seven of the 98 trajectories, corresponding to initial times $t_0 = 0.5$, 1, 2, 2.9, 4.5, 6.5, 7.5 s (t_0 being measured when the temperature $T_0 = 9$ GK), is highlighted with different colors. We adopt these seven trajectories as representative of the cooling evolution of the PNS to discuss the impact of neutrino oscillations (with and without an additional light sterile neutrino) on the nucleosynthesis in the ν-driven wind. The total ejecta mass of the 98 mass-shell trajectories is $M_{98} = 1.1 \times 10^{-2} M_\odot$.

In the network, 6300 species are included between the proton-drip line and neutron-drip line, up to the $Z = 110$ isotopes (see Wanajo et al. 2009, for more details). All the important reactions such as $\nu_e(n, p)e^-$, $\bar{\nu}_e(p, n)e^+$, (n, γ), (p, γ), (α, γ), (p, n), (α, n), (α, p), and their inverse ones are taken into account. The ν_e and $\bar{\nu}_e$ capture rates on free neutrons and protons are calculated as in Horowitz & Li (1999) and thus include recoil and weak magnetism corrections. The neutrino-induced reactions on heavy nuclei are not included since they have negligible effects (Meyer et al. 1998). The nucleosynthesis calculations start when the mass-shell temperature decreases to 9 GK, with an initial composition of free neutrons and protons with number fractions of $1 - Y_e$ and Y_e, respectively.

[5] Model Sf 21 is analogous to model Sf of Hüdepohl et al. (2010) but was computed with 21 energy bins for the neutrino transport instead of the usual 17 energy groups.

3. ELECTRON FRACTION EVOLUTION

The matter in a fluid element moving away from the PNS will experience three stages of nuclear evolution. Near the surface of the PNS, the temperature is so high that the matter is in nuclear statistical equilibrium (NSE) and nearly all of the baryons are in the form of free nucleons. As the material flows away from the PNS, it cools. When the temperature is $T < 1$ MeV, α particles begin to assemble to form heavier nuclei by $\alpha\alpha n$, 3α reactions, and subsequent captures of α particles and free nucleons.

Together with the entropy and the expansion time, a basic quantity defining the conditions for element formation (and eventually the r-process) is the excess of initially free n or p expressed by the electron fraction Y_e. It is locally defined as the ratio of the net electron (electrons minus positrons) number density, N_e, to the sum of proton number density N_p and neutron number density N_n:

$$Y_e(r) = \frac{N_e(r)}{N_p(r) + N_n(r)} = X_p(r) + \frac{X_\alpha(r)}{2} + \sum_{Z_A>2} \frac{Z_A(r)}{A(r)} X_A(r), \quad (1)$$

where X_p, X_α, and X_A are the mass fractions of free protons (p), α particles, and heavy elements ($Z_A > 2$) as functions of the radius. The charge and the mass numbers of the heavy nuclear species are Z_A and A, respectively. In all neutral media, $Y_e = Y_p$ and $Y_n = 1 - Y_e$, with Y_j being the number density of free or bound particle species j relative to baryons. The lower Y_e is, the more the environment is neutron-rich, and thus the more favorable it is for the r-process to occur (e.g., Hoffman

et al. 1997). On the other hand, $Y_e > 0.5$ implies that p-rich nuclei could be formed through the $\nu p-$process (Fröhlich et al. 2006a; Pruet et al. 2006; Wanajo 2006).

Having in mind the overall evolution of abundances with radius and time and assuming that the reactions of neutrinos on nuclei are negligible, the n/p ratio in the wind ejecta is set by β-interactions of electron neutrinos (ν_e) and electron antineutrinos ($\bar{\nu}_e$) with free n and p and their inverse reactions:

$$\nu_e + n \rightleftharpoons p + e^-, \tag{2}$$

$$\bar{\nu}_e + p \rightleftharpoons n + e^+. \tag{3}$$

Therefore the Y_e evolution depends on the energy distributions of ν_e and $\bar{\nu}_e$. Modifications of the neutrino emission properties, such as the energy spectra, due to flavor oscillations could significantly change the n/p ratio and thus Y_e in the wind.

Because of slow time variations of the outflow conditions during the PNS cooling phase, a near steady-state situation applies (Qian & Woosley 1996) and the rate of change of Y_e within an outflowing mass element can be written as in McLaughlin et al. (1996):

$$\frac{dY_e}{dt} = v(r)\frac{dY_e}{dr} \simeq \left(\lambda_{\nu_e} + \lambda_{e^+}\right)Y_n^f - \left(\lambda_{\bar{\nu}_e} + \lambda_{e^-}\right)Y_p^f, \tag{4}$$

with $v(r)$ being the velocity of the outflowing mass element, λ_i the reaction rates, and $Y_{n,p}^f$ the abundances of free nucleons.

In the free streaming limit with neutrinos propagating radially, the forward reaction rates of Equations (2) and (3) can be written in terms of the electron (anti)neutrino emission properties:

$$\lambda_{\nu_e} \simeq \frac{L_{\nu_e}}{4\pi r^2 \langle E_{\nu_e}\rangle}\langle \sigma_{\nu_e}\rangle, \tag{5}$$

$$\lambda_{\bar{\nu}_e} \simeq \frac{L_{\bar{\nu}_e}}{4\pi r^2 \langle E_{\bar{\nu}_e}\rangle}\langle \sigma_{\bar{\nu}_e}\rangle, \tag{6}$$

where L_{ν_e} and $L_{\bar{\nu}_e}$ are the luminosities of ν_e and $\bar{\nu}_e$ respectively, and $\langle E_{\nu_e}\rangle$ and $\langle E_{\bar{\nu}_e}\rangle$ the mean spectral energies.[6] The ν_e and $\bar{\nu}_e$ capture cross sections of the forward reactions (2) and (3), averaged over the corresponding ν_e and $\bar{\nu}_e$ energy spectra, are $\langle \sigma_{\nu_e}\rangle$ and $\langle \sigma_{\bar{\nu}_e}\rangle$, respectively. Including the weak magnetism and recoil corrections, the average neutrino capture cross sections are (Horowitz & Li 1999):

$$\langle \sigma_{\nu_e}\rangle \simeq k\langle E_{\nu_e}\rangle \varepsilon_{\nu_e}\left[1 + 2\frac{\Delta}{\varepsilon_{\nu_e}} + a_{\nu_e}\left(\frac{\Delta}{\varepsilon_{\nu_e}}\right)^2\right]W_{\nu_e}, \tag{7}$$

$$\langle \sigma_{\bar{\nu}_e}\rangle \simeq k\langle E_{\bar{\nu}_e}\rangle \varepsilon_{\bar{\nu}_e}\left[1 - 2\frac{\Delta}{\varepsilon_{\bar{\nu}_e}} + a_{\bar{\nu}_e}\left(\frac{\Delta}{\varepsilon_{\bar{\nu}_e}}\right)^2\right]W_{\bar{\nu}_e}, \tag{8}$$

with $k \simeq 9.3 \times 10^{-44}$ cm^2 MeV^{-2}, $\varepsilon_\nu = \langle E_\nu^2\rangle/\langle E_\nu\rangle$ ($\nu = \nu_e, \bar{\nu}_e$), $a_\nu = \langle E_\nu^2\rangle/\langle E_\nu\rangle^2$, M the nucleon mass in MeV, and $\Delta = 1.293$ MeV the neutron–proton mass difference. The weak magnetism and recoil correction factors are given by $W_{\nu_e} = \left[1 + 1.02 b_{\nu_e}\varepsilon_{\nu_e}/M\right]$ and $W_{\bar{\nu}_e} = \left[1 - 7.22 b_{\bar{\nu}_e}\varepsilon_{\bar{\nu}_e}/M\right]$, where $b_\nu = \langle E_\nu^3\rangle\langle E_\nu\rangle/\langle E_\nu^2\rangle^2$ represents the spectral shape factor for ν_e or $\bar{\nu}_e$. We point out that in Equation (8) the spectral integration was approximated by integrating over the interval $[0, \infty)$ instead of $[\Delta, \infty)$. Since the rates λ_{ν_e} and $\lambda_{\bar{\nu}_e}$ are functions of the neutrino fluxes, they can be affected by neutrino flavor conversions.

The inverse reaction rates of (2) and (3), λ_{e^-} and λ_{e^+}, are defined in analogy to the forward reaction rates:

$$\lambda_{e^-} = c \cdot \tilde{n}_{e^-} \cdot \langle \sigma_{e^-}\rangle, \tag{9}$$

$$\lambda_{e^+} = c \cdot n_{e^+} \cdot \langle \sigma_{e^+}\rangle, \tag{10}$$

with c being the speed of light. In Equation (9), $\tilde{n}_{e^-}$ is slightly modified compared to the electron number density

$$\tilde{n}_{e^-} = \frac{8\pi}{(2\pi\hbar c)^3}\cdot\int_0^\infty \frac{\epsilon^2}{1 + \exp\left[\dfrac{\epsilon - \tilde{\mu}_{e}}{k_B T}\right]}\, d\epsilon, \tag{11}$$

with $\tilde{\mu}_{e} = \mu_{e} - \Delta$ and μ_{e} the electron chemical potential. The average cross section $\langle \sigma_{e^-}\rangle$ of the inverse reaction (2) is

$$\langle \sigma_{e^-}\rangle \simeq \frac{1}{2}k\left\langle \widetilde{E}_{e^-}\right\rangle \varepsilon_{e^-}\left[1 + 2\frac{\Delta}{\varepsilon_{e^-}} + a_{e^-}\left(\frac{\Delta}{\varepsilon_{e^-}}\right)^2\right]W_{\nu_e}, \tag{12}$$

where $\varepsilon_{e^-} = \langle \widetilde{E}_{e^-}^2\rangle/\langle \widetilde{E}_{e^-}\rangle$ and $a_{e^-} = \langle \widetilde{E}_{e^-}^2\rangle/\langle \widetilde{E}_{e^-}\rangle^2$. In analogy to $\langle E_\nu^n\rangle$, $\langle \widetilde{E}_{e^-}^n\rangle$ is defined by using $\widetilde{f}_{e^-}(E) = \frac{\tilde{\xi}\cdot E^2}{1 + \exp[(E - \tilde{\mu}_{e})/k_B T]}$ for the electron distribution function with $\tilde{\xi}$ the normalization factor such that $\int \widetilde{f}_e(E)dE = 1$. In Equation (10), the positron number density is

$$n_{e^+} = \frac{8\pi}{(2\pi\hbar c)^3}\cdot\int_0^\infty \frac{\epsilon^2}{1 + \exp\left[\dfrac{\epsilon + \mu_{e}}{k_B T}\right]}\, d\epsilon, \tag{13}$$

and the positron average capture cross section is defined in the following way:

$$\langle \sigma_{e^+}\rangle \simeq \frac{1}{2}k\langle E_{e^+}\rangle \varepsilon_{e^+}\left[1 + 2\frac{\Delta}{\varepsilon_{e^+}} + a_{e^+}\left(\frac{\Delta}{\varepsilon_{e^+}}\right)^2\right]W_{\bar{\nu}_e}, \tag{14}$$

where $\varepsilon_{e^+} = \langle E_{e^+}^2\rangle/\langle E_{e^+}\rangle$ and $a_{e^+} = \langle E_{e^+}^2\rangle/\langle E_{e^+}\rangle^2$. The energy moments are calculated using the positron distribution function $f_{e^+}(E) = \frac{\xi_{e^+}\cdot E^2}{1 + \exp[(E - \mu_{e^+})/k_B T]}$, where ξ_{e^+} is the normalization factor such that $\int f_{e^+}(E)dE = 1$.

We approximate the weak magnetism and recoil corrections in Equations (12) and (14) by using W_{ν_e} and $W_{\bar{\nu}_e}$ of Equations (7) and (8) with the energy moments of the neutrinos produced by the e^+ and e^- capture reactions, fulfilling the detailed balance theorem. In Equations (12), (14) and Equations (7), (8) we have neglected the mass of the electron, m_e, since it does not make any difference in our calculations ($m_e \ll E \pm \Delta$). The rates λ_{e^-} and λ_{e^+} are given in Bruenn (1985), neglecting weak magnetism and recoil corrections (i.e., for $W_{\nu_e} = W_{\bar{\nu}_e} = 1$), but including m_e-dependent terms.

The nucleons involved in the β-reactions of Equation (4) are free. Accounting for the nucleons bound in α particles, the number fractions of free protons and neutrons can be written as functions of Y_e:

$$Y_p^f = Y_e - \frac{X_\alpha}{2} - \sum_{Z_A > 2}\frac{Z_A}{A}X_A, \tag{15}$$

[6] $\langle E_\nu^n\rangle \equiv \int E_\nu^n f(E_\nu)\, dE$, where $f(E_\nu)$ is the normalized (anti)neutrino energy spectrum. The energy spectrum that we use will be described in Section 4.

Table 1
Neutrinospheric Parameters and Electron Fractions Y_e as Functions of Postbounce Time t_0

t_0[a] (s)	R_ν[b] (10^5 cm)	Y_e[c]	$Y_{e,a}$[d]	$\Delta\overline{M}_j$[e] ($10^{-3}\ M_\odot$)	L_{ν_e}[f] (10^{51} erg s^{-1})	$L_{\bar\nu_e}$[f] (10^{51}erg s^{-1})	L_{ν_x}[f] (10^{51} erg s^{-1})	$\langle E_{\nu_e}\rangle$[g] (MeV)	$\langle E_{\bar\nu_e}\rangle$[g] (MeV)	$\langle E_{\nu_x}\rangle$[g] (MeV)	α_{ν_e}[h]	$\alpha_{\bar\nu_e}$[h]	α_{ν_x}[h]
0.5	25.0	0.0547	0.554	9.640	9.5	10.10	10.80	16.8	18.1	18.3	2.9	3.0	2.8
1.0	20.5	0.0522	0.546	0.770	7.3	8.30	7.90	15.9	17.4	17.3	3.0	2.9	2.6
2.0	17.5	0.0445	0.564	0.380	4.7	4.90	5.30	15.3	16.5	16.1	3.2	2.7	2.3
2.9	16.0	0.0323	0.566	0.110	3.3	3.40	3.70	15.8	16.3	15.7	3.1	2.3	2.5
4.5	15.2	0.0268	0.574	0.060	1.9	1.90	2.00	13.8	13.4	12.9	3.0	2.3	2.1
6.5	14.5	0.0233	0.555	0.020	1.0	0.99	1.04	12.4	11.9	11.8	2.6	2.3	2.4
7.5	14.5	0.0223	0.549	0.002	0.6	0.60	0.60	9.9	9.6	9.5	2.4	2.3	2.5

Notes.
[a] Postbounce time.
[b] Neutrinosphere radius.
[c] Electron fraction at R_ν.
[d] Asymptotic electron fraction (at $r = 3 \times 10^7$ cm).
[e] $\Delta\overline{M}$: ejecta mass of the seven representative wind trajectories.
[f] Luminosities of ν_e, $\bar\nu_e$, and ν_x, respectively.
[g] Mean energies of ν_e, $\bar\nu_e$, and ν_x, respectively.
[h] Spectral fitting parameters of ν_e, $\bar\nu_e$, and ν_x, respectively (see Section 4).

$$Y_n^f = 1 - Y_e - \frac{X_\alpha}{2} - \sum_{Z_A>2} \frac{N_A}{A} X_A, \tag{16}$$

where X_α (X_A) is the mass fraction of α particles (heavy nuclei). In Table 1, we list the Y_e values at the neutrinosphere[7] radius R_ν for the selected seven postbounce times t_0, as obtained from the numerical simulation of Model Sf 21 of Hüdepohl et al. (2010).

Since we aim to discuss the impact of neutrino oscillations and that of the so-called "α-effect" on the electron fraction and on the nucleosynthesis in the ν-driven wind, we distinguish two cases with different X_α in what follows.

(i) We compute X_α using the full network (labelled "incl. α-effect").
(ii) We keep X_α constant at its value at $T = 9$ GK as given by Model Sf 21.

The recombination of free nucleons to α particles affects Y_p^f and Y_n^f according to Equations (15) and (16), and via Equation (4) it influences the evolution of Y_e. Since the formation of α particles binds equal numbers of neutrons and protons, the remaining free nucleons will be dominated by the more abundant nucleonic species, either n or p. The corresponding capture reactions of ν_e (and e^+) on neutrons in the case of neutron excess or of $\bar\nu_e$ (and e^-) on protons for proton-rich conditions will drive Y_e closer to 0.5, which is the so-called α-effect first pointed out by McLaughlin et al. (1996) and Meyer et al. (1998). Since a proper inclusion of the α-effect always requires detailed network calculations as in our case (i), we consider case (ii) for isolating the effect of the formation of α particles on Y_e, as we will elucidate in Section 6.

3.1. Nucleosynthesis Yields without Neutrino Oscillations

Wanajo et al. (2011b) studied in detail the nucleosynthesis yields during the first 250–300 ms of the explosion of an 8.8 $M_\odot$ ECSN in 1D and 2D. In this section, we discuss as our fiducial case the results of nucleosynthesis in the subsequent ν-driven wind ejecta of the same model without taking into account neutrino oscillations (but including the α-effect). Note that nucleosynthesis computations were done in previous papers adopting semi-analytically (Wanajo et al. 2001; Wanajo 2006) or hydrodynamically (Takahashi et al. 1994; Fröhlich et al. 2006b; Pruet et al. 2006; Arcones & Montes 2011) computed neutrino-driven winds. With the exception of investigations by Meyer et al. (1992) and Woosley et al. (1994), who used the now outdated model of J. Wilson, however, the other existing calculations were based on a number of simplifications or considered only constrained periods of evolution (like Pruet et al. 2006). In this sense, our study is the first one in which the wind nucleosynthesis is explored in a self-consistently exploded progenitor, whose evolution was continuously followed from collapse to beyond the explosion through the complete subsequent PNS cooling phase. Nevertheless, the results should not be taken as firm nucleosynthetic predictions to be used for galactic chemical evolution studies because of the absence of dense-medium nucleon potential effects in the charged-current neutrino reactions of the hydrodynamic simulation. The inclusion of these nucleon-potential effects will cause nuclear equation-of-state-dependent modifications of the neutrino emission and therefore of the Y_e evolution in the ν-driven wind (e.g., Martínez-Pinedo et al. 2012; Roberts 2012; Roberts et al. 2012), whose investigation is beyond the present work.

Taking into account 98 trajectories, X_A is given by

$$X_A = \frac{1}{M_{\rm tot}} \sum_{i=1}^{98} X_{i,A}\ \Delta M_i, \tag{17}$$

where $X_{i,A}$ and ΔM_i are the mass fractions and the ejecta-shell masses respectively, while $M_{\rm tot}$ is the total mass of the ejecta, which we consider to be the sum of the ejected mass from the core plus the outer H/He envelope (assumed to contain no heavy elements):

$$M_{\rm tot} = \left(8.8\ M_\odot - 1.366\ M_\odot\right) + 0.0114\ M_\odot \simeq 7.44\ M_\odot.$$

Here 1.366 $M_\odot$ defines the initial mass cut between neutron star and ejecta and $M_{98} = 0.0114\ M_\odot$. In order to discuss the

[7] The neutrinosphere is defined as the region at which the neutrinos or antineutrinos escape from the PNS surface. We notice that, in general, the neutrinosphere R_ν is different for different (anti)neutrino flavors. We assume R_ν to be roughly the same for all flavors.

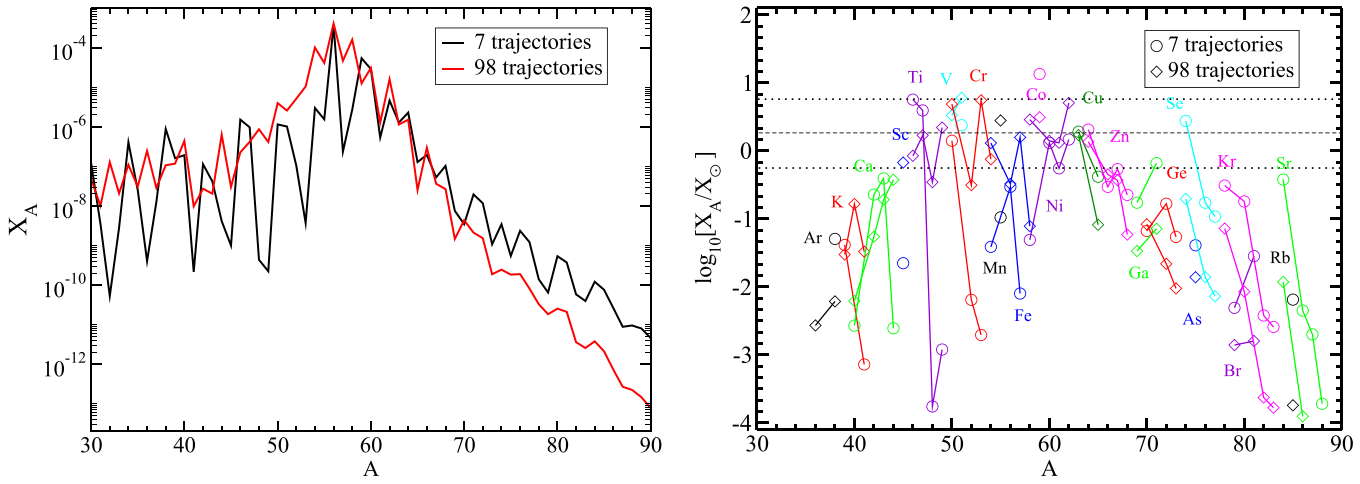

Figure 2. Left: mass fractions X_A of the ejecta as a function of mass number A comparing the cases for seven representative trajectories and for all the 98 trajectories. Right: comparison of the isotopic ejecta mass fractions (X_A) relative to the solar ones ($X_\odot$). The horizontal upper dotted line passes through the most overproduced isotopes (^{51}V, ^{53}Cr, and ^{62}Ni) in the 98 trajectory case, and the horizontal lower dotted line lies a factor of 10 below the level of the upper line. The dashed line represents the median value. Our seven selected trajectories reproduce the case with the 98 trajectories satisfactorily well only for certain values of A (e.g., $58 \leqslant A \leqslant 69$).

impact of neutrino oscillations[8] in the following sections, we replace the full set of 98 trajectories by seven "representative" ν-driven wind trajectories (Figure 1).

For the seven representative wind trajectories, we define combined mass elements, $\Delta\overline{M}_j$ ($j = 1, \ldots, 7$), in such a way that $\Delta\overline{M}_j = \sum_{i=i_{j-1}+1}^{i_j} \Delta M_i$, where the summation includes all mass shells ejected between the representative shell i_{j-1} and the representative shell i_j (see Table 1). The first representative shell, for example, includes all the 10 trajectories of the full set which are ejected before $t_0 = 0.5$ s. Thus, for the seven representative trajectories, we define

$$\overline{X}_A = \frac{1}{M_{\rm tot}} \sum_{j=1}^{7} X_{j,A}\, \Delta\overline{M}_j, \tag{18}$$

with X_j being the mass fractions for the jth trajectory.

Figure 2 shows the nucleosynthesis mass fractions, without taking into account neutrino oscillations, for the 98 trajectories and for the seven trajectories after mass integration over the ejecta mass-shell range as given by Equations (17) and (18), respectively. In the left panel, the mass fractions X_A obtained for all of the 98 available ν-driven wind trajectories are compared to the ones obtained for the seven selected trajectories. The right panel of Figure 2 shows the isotopic mass fractions X_A relative to the solar ones $X_\odot$ (Lodders 2003, i.e., the production factors) for the 98 available ν-driven wind trajectories and for the seven representative ones as functions of A. The dotted horizontal lines represent a "normalization band." The isotopes that fall into this band are considered to be the main nucleosynthetic products from the neutrino-driven wind phase of our fiducial ECSN model that could contribute to galactic chemical evolution. The upper dotted line passes through the most overproduced elements (^{51}V, ^{53}Cr, and ^{62}Ni), and the lower dotted line lies a factor of 10 below that. The middle dashed line represents the median value.

We find that the nucleosynthesis yields of the seven trajectories reproduce those obtained from all the 98 trajectories only very approximately because of the coarse time resolution of the wind history. Nevertheless, this will be qualitatively sufficient to discuss the effects of neutrino oscillations on the nucleosynthesis conditions. The right panel of Figure 2 shows little production of isotopes with $A > 65$ in the 98 trajectory case as well as in the seven trajectory case. This is a consequence of a weak νp-process[9] in this SN environment because of the absence of a dense outer stellar envelope in ECSNe, which is crucial for an efficient νp-process (Wanajo et al. 2011a). Many of the iron-group and light trans-iron isotopes still lie on the normalization band, but the greatest production factors (for ^{51}V, ^{53}Cr, and ^{62}Ni in the 98 trajectory case) are below 10. For example, the production factor of ^{62}Ni is several times smaller than the corresponding one in the early ($\lesssim$400 ms) convective ejecta, which are absent in 1D but found in the 2D counterpart of the ECSN explosion model (Wanajo et al. 2011b, 2013a). It appears, therefore, that the nucleosynthetic contribution of the ν-driven wind to the Galactic chemical evolution is unimportant. It should be noted, however, that the effects of nucleon potential corrections might alter the Y_e history; thus the wind contribution could be more important for nucleosynthesis than found here.

4. REFERENCE NEUTRINO SIGNAL AND FLAVOR EVOLUTION EQUATIONS

At radius $r > R_\nu$, the unoscillated spectral number fluxes for each flavor ν ($\nu = \nu_e, \bar{\nu}_e, \nu_x, \bar{\nu}_x$ with $x = \mu$ or τ) can be approximated by

$$F_\nu(E) \approx \frac{L_\nu}{4\pi r^2} \frac{f_\nu(E)}{\langle E_\nu \rangle}, \tag{19}$$

[8] We assume that the ν_e and $\bar{\nu}_e$ luminosities and energy spectra do not change for $r \geqslant R_\nu$. This means that we not only ignore small evolutionary changes due to remaining neutrino interactions in the external medium but we also disregard general relativistic redshift corrections, which depend on r, and which are included in the hydrodynamic simulations.

[9] In Table 1, we show the asymptotic values (indicated by subscript "a") of the electron fraction $Y_{e,\rm a}$ for our seven representative trajectories. Notice that since $Y_{e,\rm a} > 0.5$ for all the considered cases, the νp-process may be enabled.

where L_ν is the luminosity for the flavor ν and $\langle E_\nu \rangle$ the mean spectral energy.[10] The neutrino spectrum $f_\nu(E)$ is well reproduced by a combined power-law and exponential fit (Keil et al. 2003; Tamborra et al. 2012a):

$$f_\nu(E) = \xi_\nu \left(\frac{E}{\langle E_\nu \rangle} \right)^{\alpha_\nu} e^{-(\alpha_\nu+1)E/\langle E_\nu \rangle}, \quad (20)$$

the parameter α_ν being defined by $\langle E_\nu^2 \rangle / \langle E_\nu \rangle^2 = (2+\alpha_\nu)/(1+\alpha_\nu)$ and ξ_ν a normalization factor such that $\int f_\nu(E) dE = 1$.

In order to incorporate neutrino oscillations in our nucleosynthesis computations, we consider the seven selected postbounce times t_0 as representative of the changing wind conditions during the PNS cooling phase (note the partial overlap with data from the simulation by Hüdepohl et al. (2010) used for the analysis in Tamborra et al. (2012b)). In Table 1 we list the neutrinosphere radius R_ν (assumed to be equal for all flavors), the luminosity L_ν, the mean energy $\langle E_\nu \rangle$, and the fit exponent α_ν for each neutrino flavor and for the seven representative wind trajectories.

In what follows, we neglect oscillations driven by the smallest mass difference between the active flavors, $\delta m_{\rm sol}$, and focus on neutrino oscillations in the active sector driven by the largest mass difference between ν_e and ν_x, $\delta m_{\rm atm}$, and by the mixing angle θ_{13}. The reduction to two effective active flavors is justified since oscillations driven by the solar parameters tend to take place at a radius larger than the one at which oscillations driven by $\delta m^2_{\rm atm}$ occur. Flavor oscillations driven by the solar parameters are, therefore, unlikely to affect SN nucleosynthesis (see Dasgupta & Dighe 2008; Fogli et al. 2009a; Dasgupta et al. 2010 for details). Concerning active–sterile oscillations, we assume the mixing only of the electron neutrino flavor with a light sterile state for simplicity. Overall, we discuss a two-flavor scenario (two active flavors, ν_e and ν_x) as well as a three-flavor one (two active + one sterile flavors, ν_e, ν_x, and ν_s).

If interpreted in terms of sterile neutrinos ν_s, the reactor antineutrino anomaly requires a mass difference in the eV range, and cosmological hot dark matter limits imply that the sterile state would have to be heavier than the active flavors (Abazajian et al. 2012). We here adopt the following mass splittings (Mention et al. 2011; Capozzi et al. 2014):

$$\delta m^2_{\rm atm} = -2.35 \times 10^{-3}\ {\rm eV}^2 \ \text{ and } \ \delta m^2_{\rm s} = 2.35\ {\rm eV}^2, \quad (21)$$

with $\delta m^2_{\rm atm}$ being the squared mass difference between the neutrino mass eigenstates ν_3 and the remaining two $\nu_{1,2}$ (Fogli et al. 2006), and $\delta m^2_{\rm s}$ the squared mass difference between the neutrino mass eigenstate ν_4 and ν_1, chosen to be representative of reactor-inspired values. We assume normal hierarchy for the sterile mass-squared difference, namely $\delta m^2_{\rm s} > 0$ (i.e., the neutrino mass eigenstate ν_4 is heavier than the other mass eigenstates associated to the active neutrino flavors) and inverted mass hierarchy for the atmospheric difference, $\delta m^2_{\rm atm} < 0$ (meaning that the neutrino mass eigenstate ν_3 is lighter than $\nu_{1,2}$; see Fogli et al. 2006). Note that current global fits of short-baseline neutrino experiments estimate $0.82 \leqslant \delta m^2_{\rm s} \leqslant 2.19\ {\rm eV}^2$ at a 3σ confidence level (Giunti et al. 2013), which is lower than our adopted reference value (Mention et al. 2011). Our conservative choice favors a comparison with previous results discussed in Tamborra et al. (2012b) besides not qualitatively changing our conclusions. We choose to scan only the inverted hierarchy scenario in the active sector (i.e., $\delta m^2_{\rm atm} < 0$), since this is the case where the largest impact due to collective flavor oscillations on nucleosynthesis is expected (Hannestad et al. 2006; Fogli et al. 2007, 2008; Dasgupta et al. 2010). The associated "high" (H) and sterile (S) vacuum oscillation frequencies are then

$$\omega_{\rm H} = \frac{\delta m^2_{\rm atm}}{2E} \ \text{ and } \ \omega_{\rm S} = \frac{\delta m^2_{\rm s}}{2E}, \quad (22)$$

with E being the neutrino energy. For the mixing angles we use (Mention et al. 2011; Capozzi et al. 2014)

$$\sin^2 2\theta_{14} = 10^{-1} \ \text{ and } \ \sin^2 \theta_{13} = 2 \times 10^{-2}. \quad (23)$$

We treat neutrino oscillations in terms of matrices of neutrino densities ρ_E for each energy mode E. The diagonal elements of the density matrices are related to the neutrino densities, while the off-diagonal ones encode phase information. The radial flavor evolution of the neutrino flux is given by the "Schrödinger equations,"

$$i\partial_r \rho_E = \left[\mathsf{H}_E, \rho_E \right] \ \text{ and } \ i\partial_r \bar{\rho}_E = \left[\bar{\mathsf{H}}_E, \bar{\rho}_E \right], \quad (24)$$

where an overbar refers to antineutrinos and sans-serif letters denote 3×3 matrices in the (ν_e, ν_x, ν_s) flavor space. The initial conditions for the density matrices are $\rho_E = {\rm diag}(n_{\nu_e}, n_{\nu_x}, 0)$ and $\bar{\rho}_E = {\rm diag}(n_{\bar{\nu}_e}, n_{\bar{\nu}_x}, 0)$, i.e., we assume that sterile neutrinos are generated by flavor oscillations. The Hamiltonian matrix consists of the vacuum, matter, and neutrino self-interaction terms:

$$\mathsf{H}_E = \mathsf{H}^{\rm vac}_E + \mathsf{H}^{m}_E + \mathsf{H}^{\nu\nu}_E. \quad (25)$$

In the flavor basis, the vacuum term,

$$\mathsf{H}^{\rm vac}_E = \mathsf{U}\ {\rm diag}\left(-\frac{\omega_{\rm H}}{2}, +\frac{\omega_{\rm H}}{2}, \omega_{\rm S} \right) \mathsf{U}^\dagger, \quad (26)$$

is a function of the mass-squared differences (with U being the unitary matrix transforming between the mass and the interaction basis) and of the mixing angles. The matter term spanned by (ν_e, ν_x, ν_s) is in the flavor basis

$$\mathsf{H}^{m} = \sqrt{2} G_{\rm F}\ {\rm diag}\left(N_e - \frac{N_n}{2}, -\frac{N_n}{2}, 0 \right), \quad (27)$$

with N_e the net electron number density and N_n the neutron density. Using Equation (1), the matter term becomes

$$\mathsf{H}^{m} = \sqrt{2} G_{\rm F} N_b\ {\rm diag}\left(\frac{3}{2}Y_e - \frac{1}{2}, \frac{1}{2}Y_e - \frac{1}{2}, 0 \right), \quad (28)$$

being N_b the baryon density. Note that the matter potential can be positive or negative and for $Y_e > 1/3$ ($Y_e < 1/3$) a ν_e–ν_s ($\bar{\nu}_e$–$\bar{\nu}_s$) MSW resonance can occur (Mikheyev & Smirnov 1985; Nunokawa et al. 1997; McLaughlin et al. 1999; Fetter 2000). Because of Equation (28), neutrinos feel a different matter potential as Y_e changes and, at the same time, Y_e is affected by neutrino oscillations via Equation (4).

The $\mathsf{H}^{\nu\nu}$ term describes ν–ν interactions and vanishes for all elements involving sterile neutrinos (Sigl & Raffelt 1993), i.e.,

[10] In Equation (19), general relativistic redshift corrections, which depend on r, as well as a "flux factor" accounting for nonradial neutrino momenta close to the neutrinosphere are ignored.

$\mathsf{H}^{\nu\nu}_{es} = \mathsf{H}^{\nu\nu}_{xs} = \mathsf{H}^{\nu\nu}_{ss} = 0$ (i.e., the only non-vanishing off-diagonal element of the 3×3 matrix is $\mathsf{H}^{\nu\nu}_{ex}$). In the treatment of ν–ν interactions, we assume the so-called "single-angle approximation" for the sake of simplicity, i.e., we assume that all neutrinos feel the same average neutrino–neutrino refractive effect (Duan et al. 2006; Fogli et al. 2007; Duan et al. 2010). We will discuss in the following the limits of such an approximation (see Section 8).

In what follows, we explore the impact of active–active and active–sterile neutrino conversions on the nucleosynthesis conditions and nucleosynthetic yields for the seven representative trajectories corresponding to postbounce times t_0. We distinguish two scenarios.

1. "Active" case, referring to neutrino oscillations in the active sector (two active states).
2. "Sterile" case, meaning neutrino oscillations in the active and sterile sectors (two active states + one sterile state).

The coupled equations of the neutrino flavor evolution (Equations (24)) were discretized in the energy range 1–60 MeV and solved by numerical integration together with Equation (4) at each selected t_0.[11] The initial conditions for the electron fraction and the neutrino spectral properties were assumed as given in Table 1.

5. NEUTRINO OSCILLATIONS IN THE NEUTRINO-DRIVEN WIND AND FEEDBACK ON THE ELECTRON FRACTION

In this section, we discuss the neutrino flavor oscillation physics during the neutrino-driven wind phase and the oscillation feedback on Y_e for scenarios 1 and 2 (see Section 4). After qualitatively describing the oscillation phenomenology, we will discuss in detail how the neutrino fluxes are affected by flavor oscillations at three representative times $t_0 = 0.5$, 2.9, and 6.5 s, representing the early, intermediate, and late cooling phases, respectively. We will focus on the impact of flavor oscillations on Y_e, neglecting the α-effect for the sake of simplicity (i.e., X_α is assumed to be as in case (ii) in Section 3); The impact of the α-effect on the electron fraction and its interplay with neutrino oscillations will be described in Section 6.

5.1. Neutrino Oscillation Phenomenology

In the presence of only active neutrinos, the MSW resonance due to the atmospheric mass difference occurs at radii much larger than the ones considered here ($r \lesssim 3 \times 10^7$ cm), where Y_e has already reached its asymptotic value, and therefore the electron fraction is not affected. Because of ν–ν interactions, multiple spectral splits should occur in inverted hierarchy for the initial conditions of neutrinos and antineutrinos of the studied ECSN (i.e., $L_{\nu_e,\bar{\nu}_e}/\langle E_{\nu_e,\bar{\nu}_e}\rangle - L_{\nu_x}/\langle E_{\nu_x}\rangle < 0$; Fogli et al. 2009b). However, since the ν_e and $\bar{\nu}_e$ luminosities and mean energies are very similar to those of the heavy-lepton neutrinos, as shown in Table 1, and because of the total lepton-number conservation, we do not expect any appreciable variations in the oscillated luminosities and mean energies (see Fogli et al. 2009b for an extended discussion).

In the sterile scenario, while active neutrinos propagate away from the SN core, they interact with the matter background and convert to sterile states through MSW resonances in two different spatial regions (see also the Appendix). Close to the neutrinosphere, due to the steep growth of Y_e, and therefore of the matter potential via Equation (28), the inner active–sterile MSW resonance occurs for both neutrinos and antineutrinos at about the same radius ($r_{\rm IR}$). At larger radii (located closer to the neutrinosphere as the postbounce time increases), an outer active–sterile MSW resonance occurs and it mainly affects neutrinos. Any modification of the neutrino energy spectra due to oscillations will affect the electron fraction via Equations (4)–(6).

At early postbounce times, the matter potential felt by neutrinos close to $r_{\rm IR}$ is slightly less steep than the one felt by antineutrinos (see the Appendix and left panel of Figure 6), therefore the adiabaticity of the $\bar{\nu}$ conversions is slightly decreased and that of ν slightly increased with a net conversion probability for neutrinos a bit larger than for antineutrinos, as pointed out by Nunokawa et al. (1997). This is particularly evident during the accretion phase as discussed in Wu et al. (2014) and, for our purposes, during the early cooling phase ($t_0 = 0.5$, 1 s), where the difference in the conversion probabilities of ν_e and $\bar{\nu}_e$ is responsible for a plateau in the Y_e profile close to $r_{\rm IR}$ (Wu et al. 2014). As the postbounce time increases, the matter potential felt by neutrinos close to $r_{\rm IR}$ becomes steeper (see Figure 6, left panel), and therefore the $\nu_e \rightarrow \nu_s$ and $\bar{\nu}_e \rightarrow \bar{\nu}_s$ resonant conversions are expected to have roughly the same degree of adiabaticity, with a resultant small feedback effect on Y_e (assuming that further flavor conversions due to ν–ν interactions are negligible).

The outer active–sterile MSW resonance is generally more adiabatic than the inner one: It occurs where the matter potential is shallow and the effective mixing angle is larger. Therefore, ν_e are abundantly converted to ν_s, lowering the wind Y_e (via Equations (4)–(6)).

Besides neutrino interactions with matter, neutrino self-interactions affect the neutrino oscillated fluxes, and therefore Y_e (see the Appendix for more details). As discussed in Tamborra et al. (2012b), $\nu_e \leftrightarrow \nu_x$ conversions, due to neutrino–neutrino interactions, partially repopulate the electron sector depleted by $\nu_e \rightarrow \nu_s$ MSW conversions. The net effect is that ν–ν interactions favor the repopulation of the ν_e sector (because of ν_x–ν_e conversions) and partially counterbalance the effect of the ν_e–ν_s MSW resonances on the electron fraction. The role played by neutrino self-interactions becomes more and more evident as the time t_0 increases, since the matter background is lower.

5.2. Results: Neutrino Oscillations and Feedback on the Electron Fraction

In order to quantitatively describe the impact of flavor oscillations on the Y_e evolution as t_0 increases, we select three representative postbounce times, $t_0 = 0.5$, 2.9, and 6.5 s, and discuss the oscillation phenomenology in the active and sterile cases.

Figure 3 (left panel) shows the luminosities and mean energies for ν_e and $\bar{\nu}_e$ as functions of the radius in the active and sterile cases at $t_0 = 0.5$ s. As expected, in the active case, neutrino oscillations do not visibly modify the mean energies and the luminosities in the radial regime where Y_e is still evolving (i.e., $r \lesssim 2 \times 10^7$ cm). To demonstrate the effect of

[11] Note that, for simplicity, in our computations we consider the effects of energy-dependent features of the oscillated neutrino spectra on the Y_e evolution in an integral sense by adopting neutrino spectral quantities averaged over energy in Equations (7) and (8).

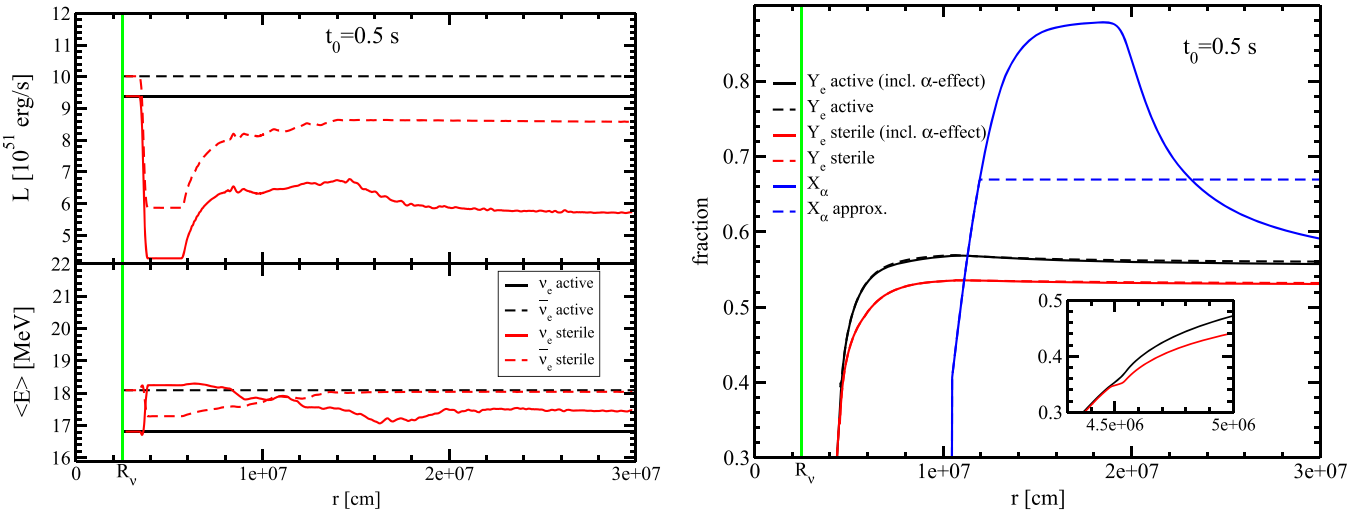

Figure 3. Left: electron neutrino and antineutrino luminosities (L_{ν_e} and $L_{\bar{\nu}_e}$) in units of 10^{51} erg s^{-1} (upper panel) and mean energies (E_{ν_e} and $E_{\bar{\nu}_e}$, lower panel) as functions of the distance (r) from the center of the PNS at $t_0 = 0.5$ s postbounce. (The solid red lines are computed as running averages over $\Delta r \simeq 3.5 \times 10^5$ cm.) In the active case the luminosities and mean energies of both ν_e and $\bar{\nu}_e$ are constant for $r \geqslant R_\nu$, which implies that the active case does not show any significant variations compared to the case without ν oscillations for the studied ECSN progenitor. In the sterile case, the inner active–sterile MSW resonance occurs for ν and $\bar{\nu}$ at $r \simeq 4 \times 10^6$ cm. Visible modifications of the neutrino spectral properties due to neutrino self-interactions occur at 6×10^6 cm, while the outer MSW resonance occurs at about 1.4×10^7 cm. Right: electron fraction Y_e and α mass fraction X_α as functions of distance r from the center of the PNS at $t_0 = 0.5$ s. In the active scenario neutrino oscillations negligibly affect Y_e (the same as in the no-oscillations case, which is not shown here). The solid lines ("incl. α-effect" cases) refer to Y_e obtained when full network calculations are performed (the corresponding X_α is also shown with the solid blue line), while the dashed Y_e lines refer to calculations corresponding to case (ii) in Section 3 (the corresponding X_α is also shown by a dashed blue line). The existence of the plateau in the Y_e profile is shown in the inset of the right panel. The vertical line shows the neutrinosphere radius R_ν.

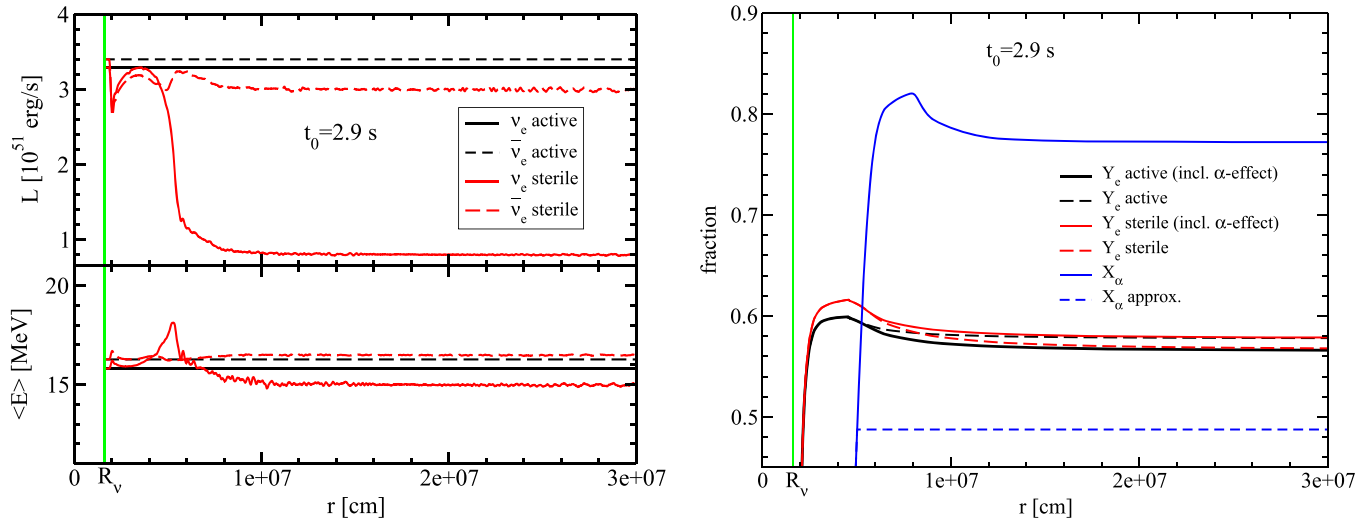

Figure 4. Same as Figure 3, but at $t_0 = 2.9$ s. In the sterile case, the inner active–sterile MSW resonance occurs for ν and $\bar{\nu}$ at $r \simeq 2 \times 10^6$ cm. The outer MSW resonance occurs at about 5×10^6 cm. (The solid red lines are computed as running averages over $\Delta r \simeq 2.9 \times 10^5$ cm.)

neutrino oscillations on Y_e, we plot Y_e as a function of the radius at $t_0 = 0.5$ s in Figure 3 (right panel). In the active case, the Y_e evolution does not differ from the case without neutrino oscillations. In the sterile case, instead, the inner active–sterile MSW resonance occurs at $r_{\rm IR} \simeq 4 \times 10^6$ cm and leads to the formation of a small plateau in the Y_e profile (see zoom in the right panel of Figure 3). In fact, the inner resonance is responsible for a $\nu_e \rightarrow \nu_s$ conversion probability larger than the $\bar{\nu}_e \rightarrow \bar{\nu}_s$ one, as expected (Figure 3, left panel). Such active–sterile flavor conversion modifies the ν_e and $\bar{\nu}_e$ energy spectra, introducing non-zero off-diagonal terms in the neutrino density matrices. Neutrino self-interactions are therefore triggered at about 6×10^6 cm. The outer active–sterile MSW resonance occurs at $r_{\rm OR} \simeq 1.4 \times 10^7$ cm, converting ν_e to ν_s. The corresponding electron fraction (Figure 3, right panel) shows a very small plateau corresponding to $r_{\rm IR}$ and it remains lower than in the active case due to active–sterile flavor conversions.

Figure 4, analogously to Figure 3, shows the luminosities and mean energies for ν_e and $\bar{\nu}_e$ as functions of the radius at $t_0 = 2.9$ s (left panel) and the corresponding electron fraction (right panel). In the active case, neutrino oscillations do not visibly modify the neutrino spectral properties in the radial regime where Y_e is still evolving, as already discussed at $t_0 = 0.5$ s. In the sterile case, the inner active–sterile MSW resonance occurs at $r_{\rm IR} \simeq 2 \times 10^6$ cm. As discussed in the Appendix, the instability induced by the inner MSW resonance and the fact that the matter potential is lower than at earlier postbounce times trigger neutrino self-interactions converting

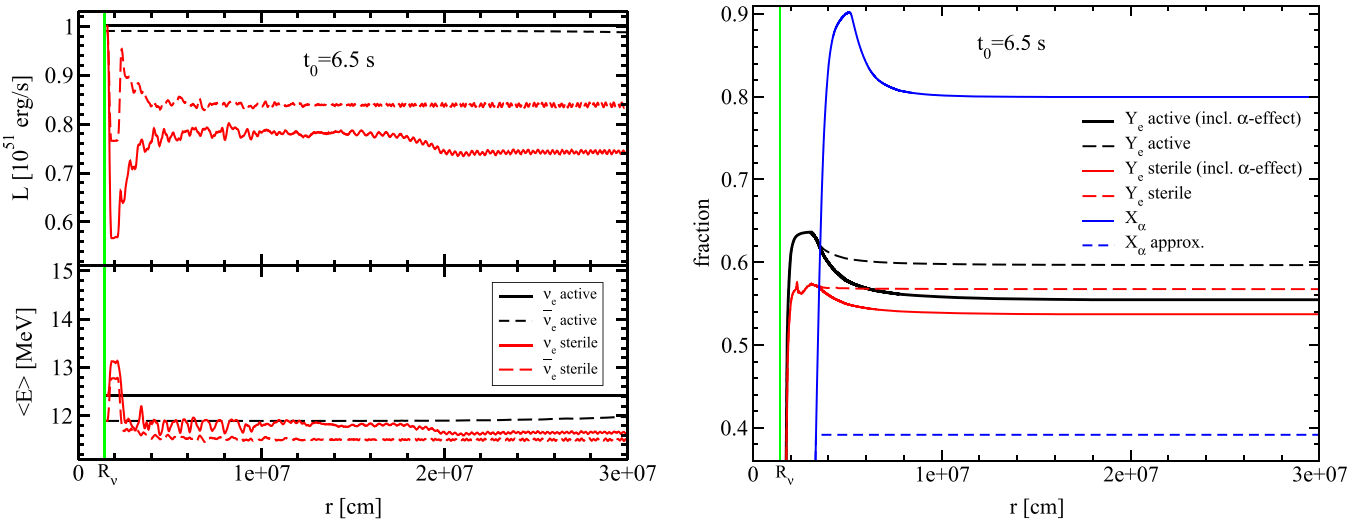

Figure 5. Left: same as Figure 3, but at $t_0 = 6.5$ s. In the sterile case the inner MSW resonance occurs for ν and $\bar{\nu}$ at $r \simeq 1.8 \times 10^6$ cm. The outer ν_e–ν_s MSW takes place at $r \simeq 2.5 \times 10^6$ cm. (The red lines display running averages over $\Delta r \simeq 2.1 \times 10^5$ cm.)

slightly more $\bar{\nu}_e$ than ν_e, contrarily to what is expected. The outer active–sterile MSW resonance occurs at about $r_{\rm OR} \simeq 5 \times 10^6$ cm, converting a large number of ν_e to ν_s. Correspondingly, the Y_e profile (Figure 4, right panel) is higher than the active one close to the neutrinosphere (because more $\bar{\nu}_e$ are converted to sterile states than ν_e). The depletion of the ν_e flux due to the outer MSW resonance is responsible for lowering the electron fraction below the active one (compare the black dashed line to the red dashed line).

Figure 5 shows the radial evolution of the ν_e and $\bar{\nu}_e$ spectral properties and the corresponding Y_e profile at $t_0 = 6.5$ s. In this case as well, active neutrino oscillations do not change the values of the luminosities and mean energies, and therefore Y_e does not change compared to the case without oscillations. In the sterile case, instead, the inner MSW resonance already occurs at $r \simeq 1.8 \times 10^6$ cm for ν and $\bar{\nu}$, triggering at the same time neutrino collective oscillations, while the outer MSW resonance takes place at $r_{\rm OR} \simeq 2.5 \times 10^6$ cm (see the Appendix for more details). Finally, flavor conversions among the active flavors slightly modify the luminosity and mean energy of ν_e at $r \simeq 2 \times 10^7$ cm, without affecting the survival probabilities (see Figure 12). The MSW resonances together with ν–ν interactions significantly reduce the ν_e number flux (i.e., $L_{\nu_e}/\langle E_{\nu_e}\rangle$) compared to the $\bar{\nu}_e$ number flux. This means that a more neutron-rich environment (i.e., a lower Y_e) is favored compared to the active case (see Figure 5, right panel).

6. INTERPLAY OF NEUTRINO OSCILLATIONS AND α-EFFECT ON THE ELECTRON FRACTION

In this section, we discuss the evolution of Y_e as a function of radius at our selected postbounce times ($t_0 = 0.5$, 1, 2, 2.9, 4.5, 6.5, and 7.5 s), for the scenarios 1 and 2 described in Section 4, and with the two different assumptions made in Section 3 about the evolution of the mass fraction of α particles. These assumptions allow us to disentangle the role played by neutrino oscillations from that of the α-effect in determining Y_e.

The evolution of the electron fraction is not just influenced by the ν_e and $\bar{\nu}_e$ properties, which are affected by neutrino oscillations, as discussed in the previous section, but also by the presence of α particles (see Equations (4)–(6)). Therefore, the whole Y_e evolution is a complicated interplay between neutrino oscillations and the α-effect. The outcome depends on the location of the region of active–sterile conversions relative to that of the α particle formation. For this reason, we choose to analyze the evolution of Y_e in detail at three representative postbounce times, $t_0 = 0.5$, 2.9, and 6.5 s.

In Figure 3 (right), we show the evolution of Y_e at $t_0 = 0.5$ s, in the active and sterile cases and with ("incl. α-effect" case) or without the inclusion of the α-effect. In this case, the formation of α particles does not play any significant role in determining Y_e, because the formation of α particles (solid blue line) occurs when Y_e has almost reached its asymptotic value (compare the solid and dashed lines).

At intermediate and late postbounce times, the results of simulations with and without α particle formation from free nucleons have to be distinguished, because the α-effect associated with the presence of large abundances of α particles has severe consequences for the Y_e evolution. In Figure 4 (right), we show the evolution of Y_e at $t_0 = 2.9$ s, analogously to Figure 3 (right). In this case, the formation of α particles occurs when Y_e is still evolving and it overlaps with the region where the outer MSW resonance takes place (see Figure 4, left).

The results with the α-effect (solid red and black lines in Figure 4, right) show a counterintuitive behavior. While for active flavor oscillations the α-effect drives Y_e closer to 0.5 in the usual way (compare the black dashed and solid lines in Figure 4, right), the sterile neutrino case exhibits the opposite trend: In the presence of a higher abundance of α particles, i.e., despite the α-effect, Y_e remains higher and the evolution toward $Y_e = 0.5$ is clearly damped (red solid line in comparison to red dashed line). The formation of a larger abundance of α particles thus obviously reduces the influence of the active–sterile ν_e–ν_s conversions on Y_e. This astonishing result is a consequence of the fact that the conversion to sterile neutrinos occurs slightly outside (or overlaps with) the region where the rapid recombination of neutrons and protons to α particles takes place. In such a situation the influence of the ν_e–ν_s conversion on the Y_e evolution is diminished by the lower number fractions of free neutrons and protons, which lead to a lower rate of change of Y_e according to Equation (4). Instead of undergoing reactions with ν_e or $\bar{\nu}_e$, the majority of free nucleons

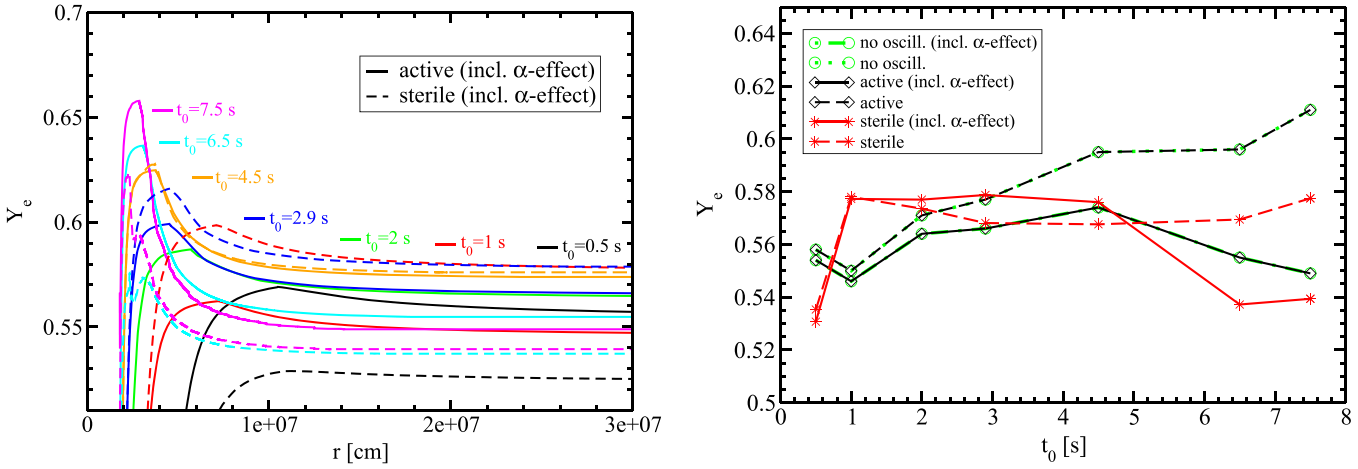

Figure 6. Left: electron fraction (Y_e) as a function of the distance r from the center of the PNS at all considered postbounce times (t_0), and in the active and sterile cases. The α-effect is included in all cases ("incl. α-effect"). Because of the near equality of the neutrino luminosities and mean energies of neutrinos of all flavors, Y_e in the active cases does not appreciably differ from the one obtained without neutrino oscillations. Right: asymptotic electron fractions (Y_e) as functions of postbounce time (t_0) in the active and sterile as well as no-oscillations cases. The dashed lines refer to Y_e calculated without the α-effect, while the solid lines refer to Y_e calculated with the full network. The α-effect is stronger especially at late times ($t_0 = 6.5$ and 7.5 s) when the neutron star is more compact and the neutrino luminosities are lower. The values in the cases without oscillations coincide with those in the active cases and cannot be distinguished.

react to form α particles as the wind expands away from the ν_e–ν_s conversion radius.

The influence of α particle formation manifests itself differently in the late wind evolution, where ν_e conversions to sterile neutrinos take place closer to the neutrinosphere and, in particular, at a radius that is smaller than the one at which nucleon recombination begins to raise the α abundance.

In Figure 5 (right), we display the evolution of the electron fraction Y_e at $t_0 = 6.5$ s, in the active and sterile cases, in analogy to Figure 4 (right).

In the sterile case, Y_e is lower than in the active case already very close to the neutrinosphere where the matter is still in NSE (and thus no α particles are present). The dashed lines are again calculated without the α-effect, while the solid lines include the α-effect.

When the α-effect is included, the value of Y_e is, as expected, pushed toward 0.5 in both active (black solid line) and sterile cases (red solid line). We notice that at $t_0 = 6.5$ s, differently from $t_0 = 2.9$ s, neutrino oscillations, in particular both the inner and outer MSW resonances, take place *before* α particles start forming, and therefore they make the environment significantly less proton-rich (Y_e is lowered) before the α-effect takes place and decreases Y_e even further toward more symmetric conditions ($Y_e = 0.5$) in the usual way.

Figure 6 gives an overview of the interplay between neutrino oscillations and the α-effect by showing the evolution of the electron fraction Y_e at all considered postbounce times t_0.

Figure 6 (left) shows Y_e as a function of the distance r from the center of the PNS at different postbounce times t_0 in both the active and sterile cases and including the α-effect.

In Figure 6 (right) the asymptotic Y_e values (namely, Y_e at $r \simeq 3 \times 10^7$ cm) are plotted as functions of the postbounce time for each of the considered scenarios (active, sterile, and no-oscillations cases). Note that the values in the active case cannot be distinguished from those in the no-oscillations case, suggesting essentially negligible roles of the active–active oscillations in the evolution of Y_e (see discussion in Section 5).

Furthermore, in the active case, Y_e is systematically pushed toward 0.5 by the α-effect, as we can see by comparing the black dashed line with the black solid one ("incl. α-effect" cases). In the sterile case (red solid line), neutrino oscillations combined with the α-effect lead to Y_e being lower than in the active case (black solid line) at early postbounce times ($t_0 = 0.5$ s), higher than in the active case at intermediate postbounce times ($t_0 = 1$, 2, and 2.9 s), and again lower than in the active case at late postbounce times ($t_0 = 6.5$ and 7.5 s).

In particular, at late times, Y_e in the sterile case and including the α-effect becomes lower than Y_e in the active case and lower than Y_e in the case without full α recombination, because both MSW ν_e–ν_s conversions happen so close to the neutrinosphere that the α particle formation at larger radii further enhances the reduction in Y_e associated with the presence of sterile neutrinos, although Y_e remains always higher than 0.5.

In summary, the α-effect plays an important role in lowering Y_e especially at late times ($t_0 = 6.5$ and 7.5 s). This is due to the higher entropy and the longer expansion timescale as a result of the more compact PNS with the lower neutrino luminosities, resulting in a delay of the α recombination relative to both the MSW ν_e–ν_s conversions and in a longer duration of the α-effect (see also next section for more details). However, although the α-effect has a strong impact on Y_e and therefore on the element production, it plays only a sub-leading role in the neutrino oscillations and no detectable modifications are expected for the neutrino fluxes at the Earth.

Because of the greater impact of the α-effect compared to oscillations on Y_e, especially at late times (see Figure 6, where Y_e in the active and sterile cases including the α-effect is fairly similar), we expect that the nucleosynthesis yields in the presence of oscillations are not significantly different from the cases where oscillations are not considered (see Section 3.1). This can be seen in Figure 7, where we show the nucleosynthesis yields obtained for the seven representative trajectories in the active and sterile cases relative to those without neutrino oscillations. In Figure 7 (left) we notice that most of the isotopic mass fraction ratios in the sterile case relative to the no-oscillations case are lower than 2, with the exception of some isotopes (with $A < 60$) that have enhanced production factors.

The most abundantly produced isotope in the relative comparison is ^{49}Ti ($X^{^{49}\mathrm{Ti}}_{\mathrm{sterile}}/X^{^{49}\mathrm{Ti}}_{\mathrm{no\text{-}oscill.}} \simeq 3.57 \times 10^3$). This

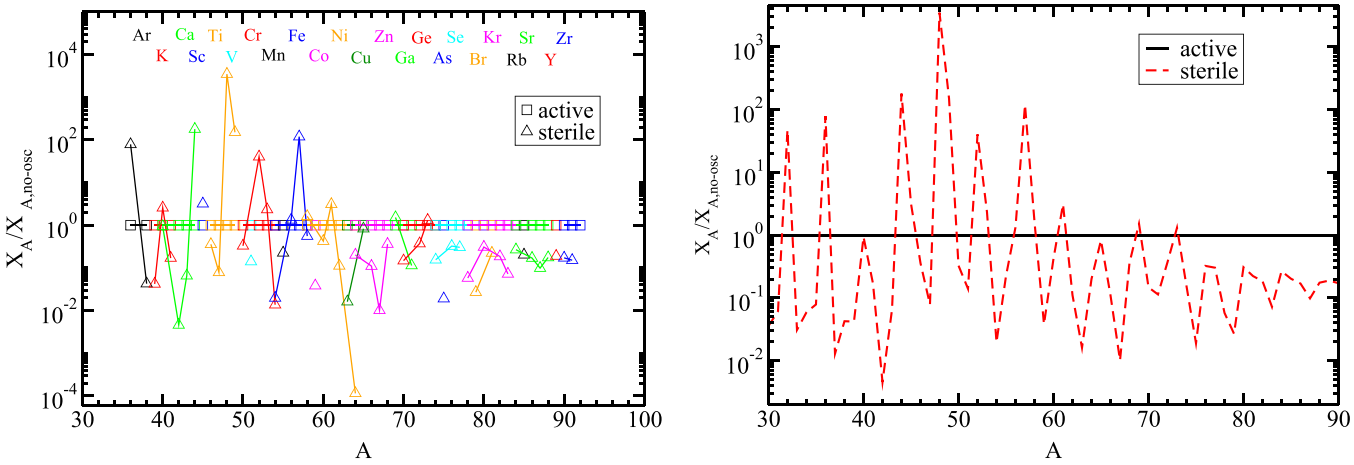

Figure 7. Left: isotopic mass fractions in the active and sterile cases relative to those in the case without oscillations vs. mass number A for all seven representative trajectories. Right: nucleosynthetic abundances in the active and sterile cases relative to those without oscillations for all seven representative trajectories. Since in our model active flavor oscillations do not change the neutrino properties and the wind Y_e at any significant level up to the radius of interest, the nucleosynthesis results are essentially identical for all the cases with active oscillations and no neutrino oscillations.

overproduction of the ^{49}Ti isotope in the sterile case compared to the case without oscillations, however, is still too small to have any significant impact on the production factor of this isotope (see Figure 2, right). From Figure 7, it is also clear that, in the sterile case, there is less production of heavy elements (e.g., $A \geqslant 70$) than in the case without oscillations.

For all the reasons above, one can conclude from Figures 6 and 7 that neither active neutrino oscillations nor a fourth sterile neutrino family can alter the nucleosynthesis-relevant conditions, nor can they create a neutron-rich site ($Y_e < 0.5$) to activate the r-process in the adopted ECSN model (without nucleon potential corrections; see Section 7).

7. NEUTRINO OSCILLATIONS IN A NEUTRON-RICH WIND

In the previous sections, we considered the neutrino emission properties in the proton-rich environment obtained in the ECSN model of Hüdepohl et al. (2010). As mentioned in Section 1, however, recent work suggests that these conditions might be valid only in the early ($t_{\rm pb} \lesssim 1$ s) and late ($t_{\rm pb} \gtrsim 3$ s) wind phases. Including mean-field nucleon potential corrections for charged-current neutrino opacities in the dense medium of the PNS (Reddy et al. 1998) can cause Y_e of the wind material to become neutron-rich (possibly down to $Y_e \simeq 0.42$–0.45, see e.g., Martínez-Pinedo et al. 2012; Roberts 2012; Roberts et al. 2012) during an intermediate evolution period, although the result is sensitively dependent on the employed nuclear equation of state. To explore the role of neutrino oscillations in such a neutron-rich environment, we construct three toy models to emulate mean-field corrections of the neutrino opacities in their effect on lowering $\langle E_{\nu_e}\rangle$ and increasing $\langle E_{\bar\nu_e}\rangle$. Each toy model case will be discussed for an intermediate postbounce time ($t_0 = 2.9$ s) and a late one ($t_0 = 6.5$ s).

7.1. Toy Model Inputs

In all toy models, we artificially prescribe the ν_e and $\bar\nu_e$ spectra by fixing the shape factors:[12] $\alpha_{\nu_e} = \alpha_{\bar\nu_e} = 4$; The neutrino spectral properties not mentioned in the following are assumed as in Table 1.

In the first toy model (T1), we choose $\langle E_{\nu_e}\rangle$ and $\langle E_{\bar\nu_e}\rangle$ in order to obtain an asymptotic electron fraction[13] including the α-effect ($Y_{e,\rm a}$), or neglecting it ($Y_{e,\rm a}^{X_\alpha=0}$), lower than 0.5 (see T1 in Table 2). We then adopt the neutrino energy spectra and the electron fraction constructed in this way as initial conditions to study the evolution of neutrino flavor and its impact on the wind Y_e. The ν_x and $\bar\nu_x$ spectral properties are unchanged (see Table 1).

Luminosities and mean energies simultaneously affect Y_e. In order to prove the robustness of the T1 results, we consider another test case (toy model 2, T2), keeping the neutrinospheric number fluxes of ν_e and $\bar\nu_e$ (i.e., the $L_\nu/\langle E_\nu\rangle$ ratios) fixed as from the hydrodynamic simulation (Hüdepohl et al. 2010) and varying both the luminosities and mean energies of ν_e and $\bar\nu_e$ in order to reproduce a neutron-rich environment in the absence of oscillations. The new initial conditions are reported in Table 2 (case T2). The third toy model (T3) is similar to T1, except that we assume $\langle E_{\nu_x}\rangle = \langle E_{\bar\nu_e}\rangle$ while leaving L_{ν_x} and α_{ν_x} as in Table 1, in order to recover the usual hierarchy among the different neutrino flavors.

7.2. Neutrino Oscillations

Figures 8 and 9 (left panels) show the luminosities and mean energies of ν_e and $\bar\nu_e$ in the active and sterile cases as functions of the radius for toy model 1.

In the active case, the initial conditions for neutrinos are different from those discussed in Section 5 at the same t_0 (i.e., here we have $L_{\nu_e}/\langle E_{\nu_e}\rangle - L_{\nu_x}/\langle E_{\nu_x}\rangle > 0$). Moreover, the new spectral parameters also prescribe larger differences between the ν_e ($\bar\nu_e$) and ν_x spectra and spectral crossings that are different from the previous cases. Bipolar oscillations due to ν–ν interactions (Fogli et al. 2008, 2009b) are then triggered at $r \simeq 2.2 \times 10^7$ cm at $t_0 = 2.9$ s and $r \simeq 1.35 \times 10^7$ cm at $t_0 = 6.5$ s. The neutrino and antineutrino luminosities and

[12] We assume the shape factors of a moderately degenerate Fermi–Dirac distribution, for which $\langle E_\nu^2\rangle/\langle E_\nu\rangle^2 \simeq 1.2$ (Horowitz & Li 1999).

[13] Note that Roberts et al. (2012) employed the approximate formula $Y_e \simeq 1/(1 + \lambda_{\bar\nu_e}/\lambda_{\nu_e})$ of Qian & Fuller (1995) for estimating the electron fraction in the wind. This formula does not account for the α-effect on Y_e.

Table 2
Toy Model Parameters Emulating Mean-field Nucleon Potential Corrections on the Neutrino Opacities[a]

Toy model	t_0[b] (s)	L_{ν_e}[c] (B s^{-1})[j]	$L_{\bar{\nu}_e}$[c] (B s^{-1})	L_{ν_x}[c] (B s^{-1})	$L_{\nu_e}/\langle E_{\nu_e}\rangle$[d] (B s^{-1})	$L_{\bar{\nu}_e}/\langle E_{\bar{\nu}_e}\rangle$[d] (B s^{-1})	$L_{\nu_x}/\langle E_{\nu_x}\rangle$[d] (B s^{-1})	$\langle E_{\nu_e}\rangle$[e] (MeV)	$\langle E_{\bar{\nu}_e}\rangle$[e] (MeV)	$\langle E_{\nu_x}\rangle$[e] (MeV)	$Y_{e,a}$[f]	$Y_{e,a}^{X_\alpha=0}$[g]	$Y_{e,a}^{act}$[h]	$Y_{e,a}^{stei}$[i]
T1	2.9	**3.30**	**3.40**	**3.70**	3.268	1.099	**1.471**	6.3	19.3	**15.7**	0.422	0.403	0.422	0.430
T1	6.5	**1.00**	**0.99**	**1.04**	1.248	0.325	**0.549**	5.0	19.0	**11.8**	0.428	0.368	0.428	0.510
T2	2.9	1.670	2.899	**3.70**	**1.303**	**1.302**	**1.471**	8.0	13.9	**15.7**	0.420	0.405	0.421	0.440
T2	6.5	0.645	1.165	**1.04**	**0.499**	**0.518**	**0.549**	8.0	14.0	**11.8**	0.431	0.380	0.431	0.486
T3	2.9	**3.30**	**3.40**	**3.70**	3.268	1.099	1.196	6.3	19.3	19.3	0.422	0.403	0.422	0.407
T3	6.5	**1.00**	**0.99**	**1.04**	1.248	0.325	0.342	5.0	19.0	19.0	0.428	0.368	0.428	0.465

Notes.
[a] In the first two cases (T1), we keep the neutrinospheric luminosities of ν_e and $\bar{\nu}_e$ as given by the hydrodynamical simulation, and do not change the luminosity and mean energy of ν_x (see Table 1). In the third and fourth cases (T2), we keep the neutrinospheric number fluxes of ν_e and $\bar{\nu}_e$ as given by the hydrodynamical simulation, and do not change the corresponding values of ν_x. In the last two cases (T3), we keep the neutrinospheric luminosities of ν_e, $\bar{\nu}_e$, and ν_x as given by the hydrodynamical simulation, and assume the same neutrinospheric mean energies for $\bar{\nu}_e$ and ν_x. Notice that in all cases we mark in bold face the unchanged hydrodynamical neutrinospheric parameters of ν_e, $\bar{\nu}_e$, and ν_x.
[b] Postbounce time.
[c] Neutrinospheric luminosities of ν_e, $\bar{\nu}_e$, and ν_x, respectively.
[d] Neutrinospheric number fluxes of ν_e, $\bar{\nu}_e$, and ν_x, respectively.
[e] Neutrinospheric mean energies of ν_e, $\bar{\nu}_e$, and ν_x, respectively.
[f] Asymptotic wind electron fraction taking into account the α-effect.
[g] Asymptotic wind electron fraction without taking into account the α-effect ($X_\alpha = 0$).
[h] Asymptotic wind electron fraction taking into account neutrino oscillations in the active sector and the α-effect.
[i] Asymptotic wind electron fraction taking into account neutrino oscillations in the active and sterile sectors as well as the α-effect.
[j] 1 Bethe = 1 B = 10^{51} erg.

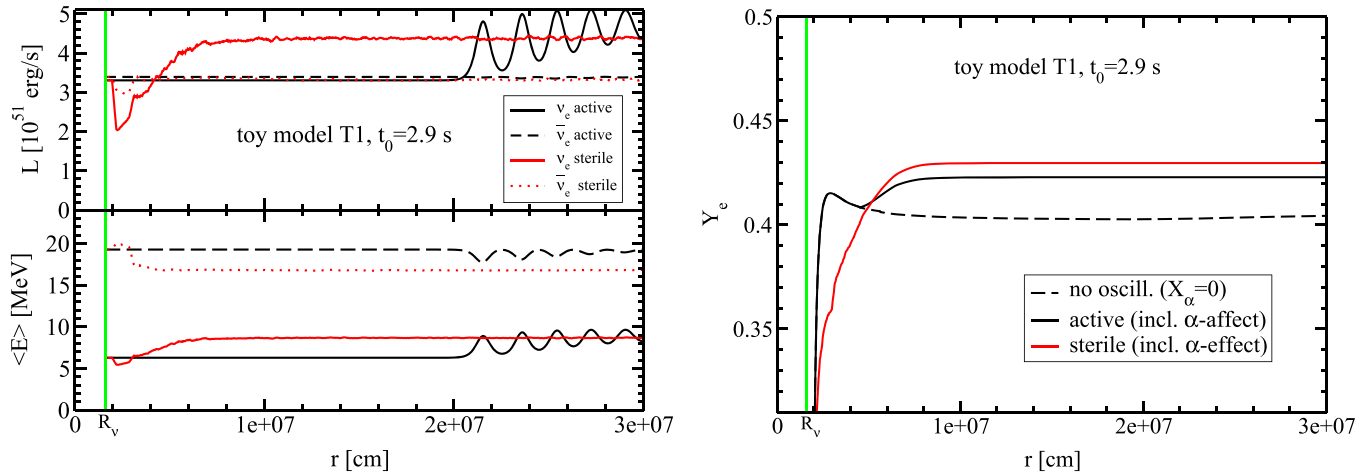

Figure 8. Left: electron neutrino and antineutrino luminosities (L_{ν_e} and $L_{\bar{\nu}_e}$ in units of 10^{51} erg s^{-1}, upper panel) for toy model 1 (see Table 2 and the text for details) as functions of the distance r from the center of the PNS, at $t_0 = 2.9$ s, in the active and sterile cases. Lower panel: similar to the upper panel but for the mean energies $\langle E_{\nu_e}\rangle$ and $\langle E_{\bar{\nu}_e}\rangle$. (The red lines are running averages over $\Delta r \simeq 1.98 \times 10^5$ cm.) Right: electron fraction Y_e as a function of the distance r from the center of the PNS for our toy model at $t_0 = 2.9$ s (see text for details) in the case without neutrino oscillations and setting $X_\alpha = 0$ ("no oscill. ($X_\alpha = 0$)" case, dashed black line), in the case with flavor conversions of active neutrinos (solid black line), and in the case of active–sterile conversions (solid red line). Both of the last two cases were computed with α particle recombination. Neutrino oscillations, jointly with the α-effect, drive Y_e toward 0.5, disfavoring the r-process.

mean energies are correspondingly modified, as shown in Figures 8 and 9 (left panels).

In the sterile case, at $t_0 = 2.9$ s (see left panel of Figure 8), the inner active–sterile MSW resonance converts both ν_e and $\bar{\nu}_e$ to sterile states. As expected, ν_e are converted slightly more abundantly to sterile states than $\bar{\nu}_e$. Soon after, the ratio $L_{\nu_e}/\langle E_{\nu_e}\rangle$ increases, and the outer active–sterile MSW resonance occurs together with neutrino self-interactions. Note that due to the feedback effect on Y_e and due to the initially lower value of Y_e compared to the corresponding standard case, the outer MSW resonance is more adiabatic and it is expected to occur at smaller radii ($r_{OR} \simeq 4 \times 10^6$ cm) than in the standard case. Moreover, due to the hierarchy of the active neutrino fluxes and due to the lower matter potential, neutrino self-interactions mix ν_e and $\bar{\nu}_e$ with the heavy lepton flavors, increasing the ν_e survival probability, differently from what is shown in Figure 4.

In the sterile case, at $t_0 = 6.5$ s (see left panel of Figure 9), the inner MSW resonance is visible as a small drop of $L_{\nu_e}/\langle E_{\nu_e}\rangle$ (and even smaller for the $\bar{\nu}_e$) at $r_{IR} \simeq 2 \times 10^6$ cm. Slightly farther outside, at $r_{OR} \simeq 2.5 \times 10^6$ cm, the outer MSW resonance occurs (similarly to the standard case). Sterile neutrinos and antineutrinos are both abundantly produced through flavor conversions due to an interplay between the

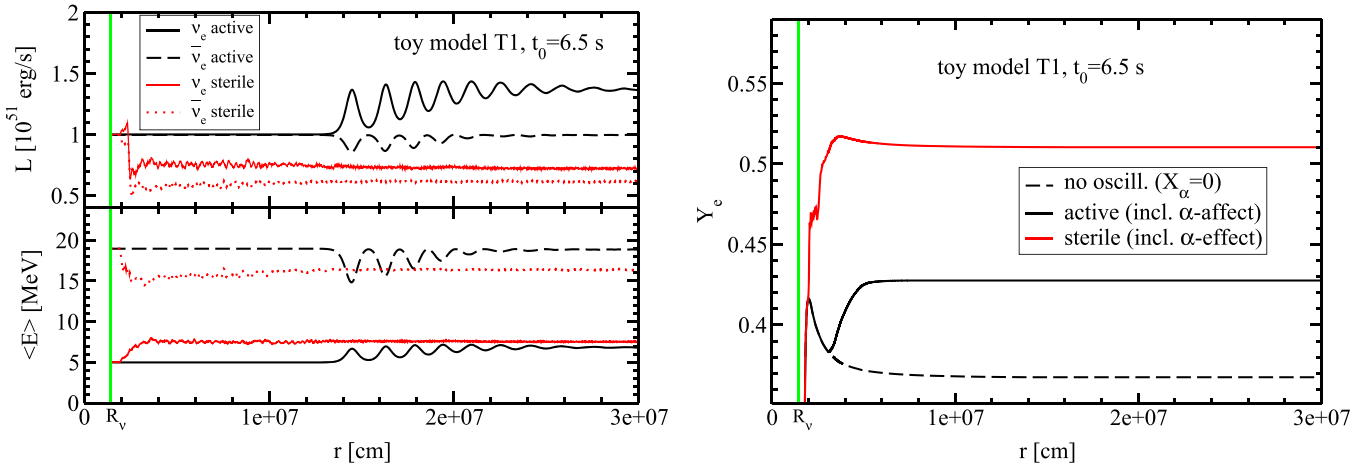

Figure 9. Same as Figure 8, but for toy model 1 at $t_0 = 6.5$ s (see the text for details). (The red lines here are running averages over $\Delta r \simeq 1.1 \times 10^5$ cm.)

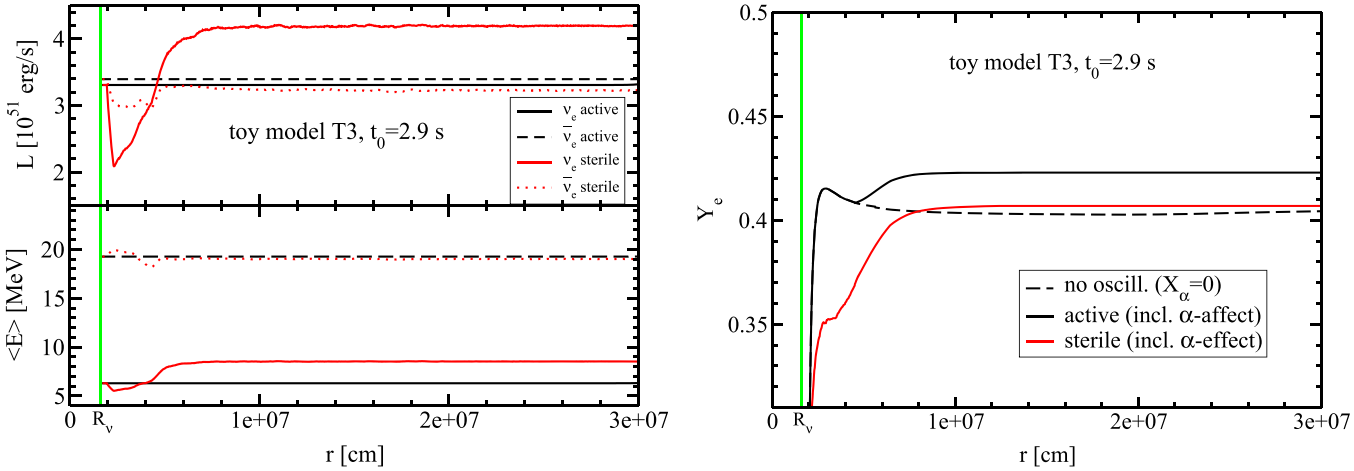

Figure 10. Same as Figure 8, but for toy model 3 (see the text for details). (The red lines here are running averages over $\Delta r \simeq 4.5 \times 10^5$ cm.)

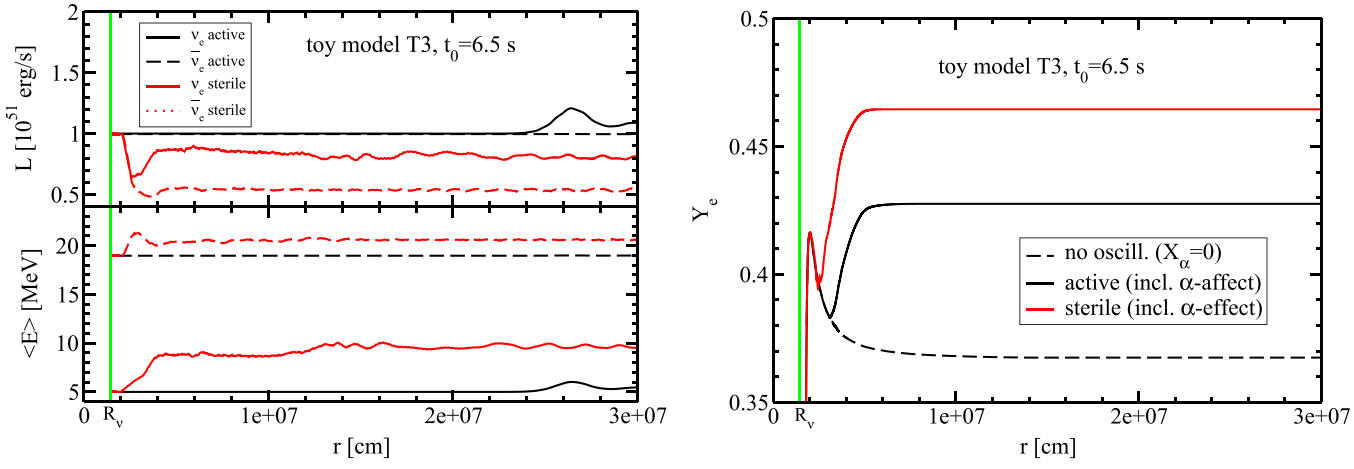

Figure 11. Same as Figure 9, but for toy model 3 (see the text for details). (The red lines here are running averages over $\Delta r \simeq 4.5 \times 10^5$ cm.)

outer MSW resonance and collective oscillations, before α particles start forming at $r \simeq 3 \times 10^6$ cm. As a consequence, both ν_e and $\bar{\nu}_e$ fluxes decrease, causing an increase of Y_e above 0.5 before the onset of the α-effect. Toy model 2 is very similar to toy model 1 concerning the oscillation phenomenology, therefore we do not show our results here and only report the corresponding neutrino emission properties and the asymptotic Y_e values in Table 2.

Toy model 3 is shown in Figures 10 and 11. In this case, the active flavors show a hierarchy of the mean energies more similar to the one reported in Table 1, although we have $L_{\nu_e}/\langle E_{\nu_e}\rangle - L_{\nu_x}/\langle E_{\nu_x}\rangle > 0$, similar to toy model T1. Therefore,

in the active case, bipolar oscillations occur at $r > 3 \times 10^7$ cm at $t_0 = 2.9$ s , while they start at $r \simeq 2.4 \times 10^7$ cm at $t_0 = 6.5$ s. In the sterile case, the inner resonance is visible at $r_{\rm IR} \simeq 2 \times 10^6$ cm at $t_0 = 2.9$ s. Soon afterwards ν–ν interactions are triggered and the ν_e survival probability starts to increase already before the region where the outer MSW resonance is expected to take place ($r_{\rm OR} \simeq 4 \times 10^6$ cm). In the sterile case, at $t_0 = 6.5$ s, the regions of the inner and outer MSW resonances almost overlap with each other, similarly to the standard case (Figure 5). This is responsible for an overall drop of $L_{\nu_e}/\langle E_{\nu_e}\rangle$ and $L_{\bar{\nu}_e}/\langle E_{\bar{\nu}_e}\rangle$.

7.3. Feedback on the Electron Fraction

In this section, we discuss the evolution of the electron fraction for toy models T1, T2, and T3 considered in the previous section in order to disentangle the impact of neutrino oscillations from that of the α-effect on Y_e in a neutron-rich neutrino-driven wind environment.

In Figures 8 and 9 (right panels), we show the evolution of Y_e at intermediate ($t_0 = 2.9$ s) and late ($t_0 = 6.5$ s) evolution phases of the neutrino-driven wind in the T1 model (see Table 2). The dashed lines refer to Y_e in the case where neither neutrino oscillations nor the α-effect are taken into account, while the solid lines display radial evolutions of Y_e, including the α-effect in the active (solid black lines) and sterile (solid red lines) cases. Since active oscillations take place at $r > 1.2 \times 10^7$ cm in both cases (i.e., after Y_e has reached its asymptotic value), the difference between $Y_{e,\rm a}^{\rm act}$ and $Y_{e,\rm a}^{X_\alpha=0}$ is just caused by the α-effect (see Table 2), which pushes Y_e toward 0.5, as expected. The impact of the α-effect on Y_e is larger at late times also in these toy models, for the reasons we already discussed in Section 6.

In the sterile case, neutrino oscillations raise the asymptotic value of the electron fraction compared to the active case, therefore the matter becomes *more proton-rich* compared to the case where oscillations are not considered or where they occur in the active sector only.

In particular, at $t_0 = 2.9$ s, the inner and outer MSW resonances in the sterile case cause Y_e to be lower than in the active case, already before α particles start forming. Then, the ν–ν interactions, which repopulate the ν_e sector, drive Y_e toward 0.5 and even above the value of Y_e in the active case, even without the α-effect, which removes free nucleons and thus moderates the impact of neutrino oscillations on Y_e, as discussed in detail in Section 6.

At $t_0 = 6.5$ s, neutrino oscillations occur very close to the neutrinosphere and push Y_e in the sterile case to a much higher value (>0.5) than in the active case, already before α particles start forming at $r \sim 4.0 \times 10^6$ cm. Therefore, the formation of α particles impacts the evolution of Y_e in the usual way, namely toward more symmetric conditions ($Y_e \longrightarrow 0.5$).

In order to prove the robustness of our conclusions about the interplay between neutrino oscillations and the α-effect, we also calculate Y_e for toy models T2 and T3. We do not show the evolution of Y_e for T2, because the discussion is very similar to T1, but we report the corresponding Y_e results in Table 2.

In the T3 active case (see black solid lines in Figures 10 and 11), the discussion about the impact of the α-effect and neutrino oscillations on the evolution of Y_e at $t_0 = 2.9$ s and $t_0 = 6.5$ s is very similar to what we already discussed in the T1 case.

In the T3 sterile case, instead, at $t_0 = 2.9$ s, we observe an interesting interplay between neutrino oscillations and the α-effect, because Y_e in the sterile case (solid red line) is lower than in the active case (solid black line), different from cases T1 and T2 at $t_0 = 2.9$ s. This is due to the fact that the MSW resonances initially deplete the number flux of ν_e in favor of ν_s much more than in cases T1 and T2, for the reasons discussed in the previous subsection. Therefore, Y_e in the sterile case is already much lower than in the active case, before α particles start forming. In the following evolution, different from cases T1 and T2, the α-effect damps the efficiency of ν–ν interactions in raising Y_e. Therefore, the latter remains lower than in the active case. However, the difference between Y_e in the active case and Y_e in the sterile case is not sufficiently large to conclude that neutrino oscillations in the sterile case make the environment significantly more neutron-rich than in the case without neutrino oscillations.

At $t_0 = 6.5$ s, we basically observe the same trend as in cases T1 and T2, namely Y_e in the sterile case is higher than in the active case. The reasons are very similar to what was already discussed for the T1 model.

In conclusion, neutrino oscillations (with or without sterile neutrinos) combined with the α-effect do not support very neutron-rich conditions in the neutrino-driven wind for the considered SN model. Conditions for a strong *r*-process in this SN progenitor are disfavored, because Y_e tends to be pushed close to 0.5 and thus the formation of a highly neutron-rich environment is prevented.

8. DISCUSSION

In this work, we studied the nucleosynthesis outcome of an ECSN with a mass of $8.8\,M_\odot$, by adopting the SN model presented in Hüdepohl et al. (2010). The same SN simulation was adopted in Tamborra et al. (2012b) to study the impact of neutrino oscillations on the electron fraction in the presence of light sterile states. However, due to the complications induced by the numerical solution of a large number of nonlinear, coupled equations with three neutrino families and the oscillation feedback on Y_e, the inner MSW resonance was not included in Tamborra et al. (2012b), assuming that its impact on the electron fraction was negligible during the neutrino-driven wind phase due to the steepness of the matter potential in that region. It was found that neutrino conversions to a sterile flavor and neutrino self-interactions influence the radial asymptotic value of Y_e in the neutrino-driven wind in complicated and time-dependent ways. These conclusions motivated us to investigate in detail the effect of oscillations on a larger variety of wind conditions and on the nucleosynthetic abundances.

In this work, the neutrino evolution is followed from the neutrinosphere outward. We also develop a more detailed treatment of the Y_e evolution than in Tamborra et al. (2012b), by accounting for the α-effect as well as recoil and weak magnetism corrections in the β processes. We find that the inner active–sterile MSW resonance has a negligible impact on Y_e during the intermediate and late cooling phases, although it modifies the ν and $\bar{\nu}$ spectra. In particular, as discussed in the Appendix, when ν–ν interactions are included, the flavor instability induced by the active–sterile MSW resonance triggers neutrino self-interactions that modify the flavor evolution history compared to the case where only interactions with the matter background are considered. On the other hand,

the inner MSW resonance induces non-negligible modifications of the electron fraction during the accretion phase, as pointed out in Wu et al. (2014), and in the early proto-NS cooling phase. It is responsible for the formation of a plateau in Y_e that drives the asymptotic value of Y_e toward smaller values.

The early cooling phase (i.e., at $t_0 = 0.5$ and 1 s) was also discussed in Wu et al. (2014) for the same ECSN progenitor, but adopting the simulation of Fischer et al. (2010). Including sterile neutrino oscillations Wu et al. (2014) obtain a neutron-rich environment ($Y_e^a[0.5\ \mathrm{s}] = 0.38$) differently from our results ($Y_e^a[0.5\ \mathrm{s}] = 0.53$, see Figures 3 and 6). Such a discrepancy might be due to the different SN models adopted as inputs in Wu et al. (2014) (i.e., Fischer et al. 2010) and in our work (i.e., Hüdepohl et al. 2010). In fact, the electron fraction without oscillations is $Y_e[0.5\ \mathrm{s}] = 0.49$ in Figure 3 (red curve) of Wu et al. (2014), while in our case it is $Y_e[0.5\ \mathrm{s}] = 0.56$ as shown in Figure 3. Our work also adopts an approach to study the electron fraction evolution different from the one employed in Wu et al. (2014) (i.e., our Equation (4) versus Equation (5) of Wu et al. 2014). The static approach of Wu et al. (2014) carries "memory" of the large modifications of the neutrino fluxes and of the electron fraction due to the inner MSW resonance at $t < 0.5$ s, while our sampling is sparse, because 90% of the ejecta of the early cooling are combined into one trajectory ejected at 0.5 s. Even adopting a denser grid in t_0, our dynamic approach should not be accurate during the accretion phase where the steady-state approximation is not applicable. Other differences on Y_e might be due to a different treatment of the neutrino oscillations. In Wu et al. (2014), a 1(active) + 1(sterile) approximation is adopted and ν–ν interactions are neglected, assuming that they are suppressed due to the high matter potential during the accretion phase (Sarikas et al. 2012), while we include the ν_e–ν_x flavor mixing as well as neutrino self-interactions in our computations.

Given the complex and nonlinear nature of neutrino self-interactions, all existing numerical studies with neutrino–neutrino refraction use simplifying assumptions. In our treatment of the neutrino evolution, we averaged the angular dependence of ν–ν interactions (the so-called "single-angle approximation," Duan et al. 2006). Because of the similarity between the ν_e and $\bar{\nu}_e$ fluxes and those of the corresponding heavy-lepton neutrinos in our hydrodynamical simulations, and because of the observed strength of the α-effect in pushing Y_e close to 0.5, even a possible relevance of multi-angle effects due to a small asymmetry among the neutrino fluxes of different flavors (Esteban-Pretel et al. 2007) is unlikely to have any significant impact on Y_e. In the sterile case, the asymmetry between ν_e and ν_x becomes even larger than in the active case due to the ν_s production, therefore we expect that a full-multi-angle treatment would only induce a smearing of the neutrino fluxes (Fogli et al. 2007), without a dramatic impact on Y_e. If the matter potential is high enough, neutrino multi-angle effects could also be responsible for a matter suppression of collective effects, and therefore produce results that are different from the ones obtained within the "single-angle" approximation (Esteban-Pretel et al. 2008). A multi-angle study was developed by Chakraborty et al. (2011) for one energy mode and for the 8.8 $M_\odot$ progenitor presented in Fischer et al. (2010): a complete matter suppression of the collective effects due to multi-angle matter effects was never achieved for this progenitor, because of the low-density matter profile. We therefore suspect that also the triggering of the collective effects induced by the inner MSW resonance instability should not be suppressed by a multi-angle treatment of the neutrino flavor oscillations during the cooling phase. Nevertheless, more accurate studies including multi-angle effects are mandatory and should be conducted for a larger sample of SN progenitors and nuclear equations of state, especially because, according to the modeling presented in Duan et al. (2011b), it was concluded that multi-angle effects among active flavors may affect the nucleosynthetic outcome under certain conditions.

Concerning the nucleosynthesis outcome, in the case without sterile neutrinos and neutrino oscillations, all relevant results can be found in Figure 3 of Wanajo et al. (2011b): there are nucleosynthetic yields for a 1D model (to be directly compared with Wu et al. 2014) and for a more realistic 2D model as well. The 2D model yields major and important differences compared to the 1D case, as in all details discussed in Wanajo et al. (2011b). The differences between the 1D nucleosynthesis result of Wanajo et al. (2011b) and Wu et al. (2014) are most probably due to differences in the mass-versus-Y_e distribution, which are probably caused by differences in the neutrino interaction processes adopted in our models compared to those of Fischer et al. (2010). Since the mass-versus-Y_e distribution is provided only by Wanajo et al. (2011b) and not by Wu et al. (2014), a detailed comparison between our and their nucleosynthesis results is not possible.

9. CONCLUSIONS

We presented neutrino oscillations and nucleosynthesis calculations for the neutrino-cooling phase of the PNS born in an 8.8 $M_\odot$ electron-capture SN, using trajectories for the ν-driven wind from 1D hydrodynamic simulations, in which a sophisticated treatment of neutrino transport was applied (Hüdepohl et al. 2010). In particular, we studied the consequences of neutrino oscillations of two active flavors driven by the atmospheric mass difference and θ_{13}, and, motivated by hints on the possible existence of light sterile neutrinos, we also discussed the role of flavor oscillations with one sterile and two active flavors. In our study neutrino–neutrino refraction effects were included, too. We chose ν_e–ν_s mixing parameters as suggested by the reactor anomaly (Mention et al. 2011). However, our conclusions remain valid also for moderate variations of the sterile mass-mixing parameters.

Our results demonstrate that the α-effect plays a crucial role when discussing the consequences of neutrino oscillations for the Y_e evolution in neutrino-driven winds. It can damp as well as enhance the Y_e-reducing impact of ν_e–ν_s conversions, depending on the radial position of the active–sterile MSW region relative to the radius where α particles form from nucleon recombination. In the late PNS cooling phase the production of sterile neutrinos via an MSW resonance takes place very close to the neutrinosphere, while a significant abundance of α particles in the wind appears only at larger distances. The Y_e reduction in the ejecta associated with the transformation of ν_e to ν_s is therefore amplified by the subsequent α-effect, driving Y_e from initial values considerably above 0.5 to an asymptotic value closer to 0.5. In the early wind phase the effect is different. Here the outer ν_e–ν_s MSW conversions occur farther away from the neutron star and exterior to (or coincident with) the formation region of α particles. The α-effect then moderates the Y_e reduction caused

by the presence of sterile neutrinos. Because of this dominance of the α-effect, the asymptotic neutron-to-proton ratio in the early wind becomes very similar in the cases with and without sterile neutrinos (whereas without the α-effect sterile neutrinos always cause a significant reduction of Y_e).

While the neutrino-driven wind of our ECSN model is well on the proton-rich side (Hüdepohl et al. 2010), equation-of-state-dependent nucleon mean-field potentials in the neutrinospheric region might lead to a considerably lower Y_e in the wind outflow (Martínez-Pinedo et al. 2011; Roberts et al. 2012). For this reason we constructed six toy model cases for the intermediate and late wind phases, in which the (unoscillated) neutrino spectra were chosen such that the neutrino-driven wind became neutron-rich with an asymptotic wind-Y_e (including the α-effect) of about 0.42–0.43, which is on the extreme side of the theoretical estimates. Including active–sterile flavor oscillations, the outflow turns, in some cases, *more proton-rich*, despite the conversion of ν_e to ν_s. This counterintuitive increase in Y_e is caused by neutrino oscillations, which modify the neutrino emission properties such that either the ν_e absorption is more strongly increased than the competing $\bar{\nu}_e$ absorption or the $\bar{\nu}_e$ absorption is more strongly reduced than the competing ν_e absorption. Our conclusion that sterile neutrinos are unlikely to help enforce neutron-rich conditions in the wind ejecta therefore seems to remain valid even when nucleon-potential effects are taken into account in future neutron-star cooling simulations.

If oscillations are disregarded, the wind ejecta in our ECSN model develop a proton excess and therefore only iron-group and some p-rich isotopes are created with small production factors (below 10), not adding any significant production of interesting isotopes to the nucleosynthesis yields computed for the early ejecta of 2D explosion models of such ECSNe (Wanajo et al. 2011b, 2013a, 2013b). When neutrino oscillations are taken into account by our simplified neutrino mixing scheme, the feedback of oscillations on Y_e is time-dependent, since it is sensitive to the detailed matter profile and neutrino fluxes. In the early ν-driven wind, the asymptotic Y_e value in the presence of a sterile family is lower than the Y_e value obtained without oscillations, although always >0.5. In the intermediate phase of the ν-driven wind Y_e in the presence of sterile neutrinos is even a bit higher than the one without oscillations. In the late ν-driven wind the asymptotic Y_e in the presence of sterile neutrinos is slightly lowered compared to the case without oscillations or to the case where oscillations in the active sector are considered. However, in our model of the neutrino cooling of the proto-neutron star born in an ECSN, the corresponding effects do not lead to any neutron excess. The changes of the nucleosynthetic output for models with (active or sterile) neutrino oscillations compared to the no-oscillations case are insignificant. It appears unlikely that viable conditions for strong r-processing can be established in the studied progenitor.

Our conclusions concern the ν-driven wind of an $8.8\,M_\odot$ progenitor. More studies of the impact of neutrino oscillations on the early-time ejecta, including multi-dimensional effects arising in hydrodynamic simulations (Wanajo et al. 2011b, 2013a) and including the effects of nucleon mean-field potentials in the neutrino opacities, are needed in order to shed light on the consequences of neutrino oscillations for the explosion mechanism and nucleosynthetic abundances (cf. Wu et al. 2014, who considered only a 1D model). Studies of a broader range of progenitor models, in particular also iron-core SNe with more massive proto-neutron stars, applying state-of-the-art neutrino oscillation physics, are also desirable to identify possible cases where favorable conditions for an r-process may be produced.

We thank Bernhard Müller and Meng-Ru Wu for useful discussions. I.T. acknowledges support from the Netherlands Organization for Scientific Research (NWO). S.W. acknowledges partial support from the RIKEN iTHES Project and the JSPS Grants-in-Aid for Scientific Research (26400232, 26400237). Partial support from the Deutsche Forschungsgemeinschaft through the Transregional Collaborative Research Center SFB/TR 7 "Gravitational Wave Astronomy" and the Cluster of Excellence EXC 153 "Origin and Structure of the Universe" (http://www.universe-cluster.de) is also acknowledged.

APPENDIX
FEEDBACK OF NEUTRINO SELF-INTERACTIONS ON THE ELECTRON FRACTION

Given the nonlinear nature of neutrino self-interactions, in this appendix we discuss the oscillation physics at the selected postbounce times $t_0 = 2.9$ and 6.5 s where ν–ν interactions significantly affect the neutrino spectral properties. In order to disentangle the role played by ν–ν interactions from that of the MSW resonances, we also discuss a simpler case obtained by switching off the neutrino self-interaction term (i.e., including matter effects only). Note that here we discuss the sterile case with the prescription (ii) in Section 3 for α particles, namely without taking into account the α-effect.

A simple quantity that can be introduced in order to have an idea about the locations of the active–sterile MSW resonances is the refractive energy difference between ν_e and ν_s caused by matter and neutrino refraction (see Section 4):

$$\begin{aligned} V_{es} &= \mathsf{H}_{ee}^{m+\nu\nu} - \mathsf{H}_{ss}^{m+\nu\nu} \\ &= \sqrt{2}\,G_{\rm F}\Big[N_b\Big(\frac{3}{2}Y_e - \frac{1}{2}\Big) \\ &\quad + 2\big(N_{\nu_e} - N_{\bar{\nu}_e}\big) + \big(N_{\nu_x} - N_{\bar{\nu}_x}\big)\Big]. \end{aligned} \tag{29}$$

We show V_{es} (Equation (29)) as a function of the radius at $t_0 = 2.9$ s in the top left panel of Figure 12. This profile already includes a self-consistent solution of Y_e. The regions where we should expect the inner and outer active–sterile MSW resonances are defined by the intersection of the V_{es} profile with the $\pm\omega_S$ lines (corresponding to the typical oscillation frequency of 15 MeV ν and $\bar{\nu}$, see Equation (22)): the MSW resonances should occur at $r_{\rm IR} \simeq 2 \times 10^6$ cm for ν and $\bar{\nu}$ and at $r_{\rm OR} \simeq 4.5 \times 10^6$ cm for neutrinos only.

In the matter background case, the $\nu_e \rightarrow \nu_s$ conversions are more abundant than the antineutrino ones, as already discussed in Section 5. Correspondingly, the electron fraction (fourth panel of Figure 12 on the left) is lower than the one in the case without oscillations. The outer resonance occurs at $r_{\rm OR} \simeq 50 \times 10^5$ cm only for neutrinos and it favors an even lower value of the electron fraction.

In the matter + ν background case, the inner MSW resonance takes place at the same radius as in the matter background case (see second and third panels on the left of Figure 12), but a slightly lower fraction of the ν_e are converted to ν_s because of $\mathsf{H}^{\nu\nu} \neq 0$. Moreover, it is clear by comparing

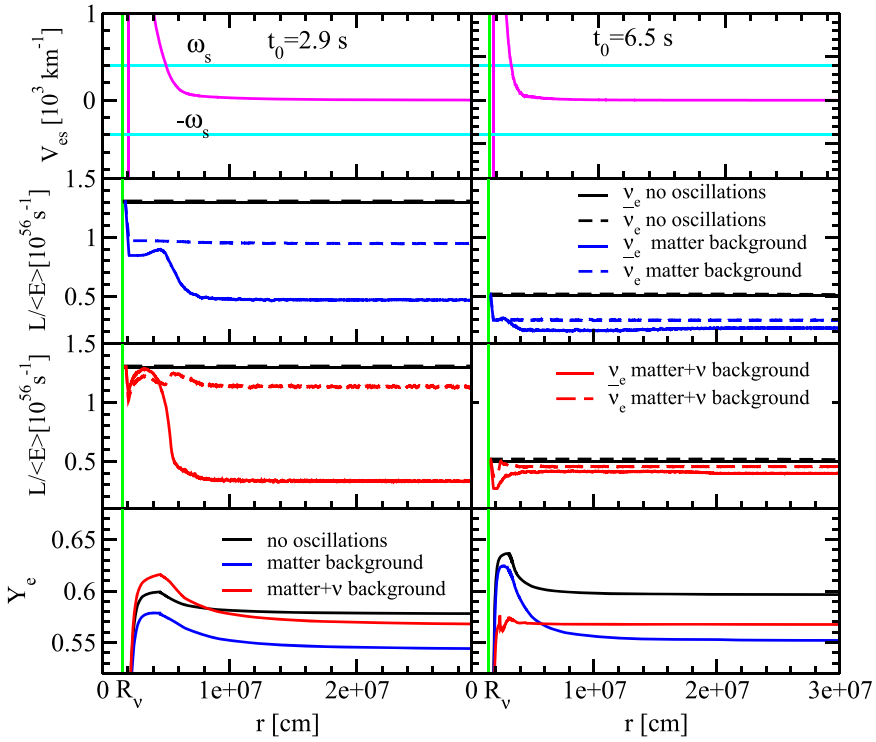

Figure 12. Top panel: refractive energy difference between ν_e and ν_s (V_{es}) in the sterile case. The horizontal lines ($\pm\omega_S$) mark the oscillation frequency of a typical energy mode of 15 MeV for neutrinos and antineutrinos. Second panel: $L_{\nu_e}/\langle E_{\nu_e}\rangle$ and $L_{\bar{\nu}_e}/\langle E_{\bar{\nu}_e}\rangle$ as functions of the distance (r) from the center of the PNS in the sterile case with matter background and in the case without oscillations. Third panel: $L_{\nu_e}/\langle E_{\nu_e}\rangle$ and $L_{\bar{\nu}_e}/\langle E_{\bar{\nu}_e}\rangle$ in the sterile case with matter + ν background and in the case without oscillations. Fourth panel: electron fraction Y_e as a function of the distance r from the center of the PNS in the matter background, matter + ν background and no-oscillation cases, without including the α-effect. The panels on the left side refer to $t_0 = 2.9$ s postbounce time, and the ones on the right to $t_0 = 6.5$ s. The vertical line marks the neutrinosphere radius R_ν.

the second and the third panels of Figure 12 that the ν–ν interaction term is responsible for replenishing the ν_e flux before the outer active–sterile MSW resonance occurs at $r_{\rm OR} \simeq 5 \times 10^6$ cm. Correspondingly, the electron fraction increases compared to the case without oscillations close to the neutrinosphere and decreases afterwards because of the outer MSW resonance. Comparing the Y_e profiles in the matter + ν background and matter background cases, we find that $Y_e(\text{matter} + \nu) - Y_e(\text{matter}) \simeq 0.025$.

The right side of Figure 12 shows the same quantities as discussed at $t_0 = 2.9$ s but at $t_0 = 6.5$ s. In the matter background case, the inner MSW resonance occurs at $r_{\rm IR} \simeq 1.8 \times 10^6$ cm as shown by the $L_{\nu_e}/\langle E_{\nu_e}\rangle$ and $L_{\bar{\nu}_e}/\langle E_{\bar{\nu}_e}\rangle$ behavior in the second panel of Figure 12 and by the top panel of the same figure. In this case, almost the same amount of ν_e and $\bar{\nu}_e$ is converted to sterile states (due to the steepness of the matter potential as discussed in Section 5). The outer MSW resonance occurs closer to the inner one than at $t_0 = 2.9$ s (at $r_{\rm OR} \simeq 2.5 \times 10^6$ cm) and it is responsible for depleting the ν_e flux in favor of sterile state production. Therefore, the electron fraction, plotted in the fourth right panel of Figure 12, becomes lower than in the case without oscillations.

In the matter + ν background case, the role played by the neutrino self-interactions is evident already close to the inner resonance. In fact, the difference between the $\nu_e \rightarrow \nu_s$ and $\bar{\nu}_e \rightarrow \bar{\nu}_s$ flavor conversions is responsible for lowering Y_e compared to the case without oscillations and with matter background only. Soon afterwards, and in correspondence to the outer resonance, the interplay between the matter and neutrino background and the nonlinear effects due to ν–ν interactions is responsible for partially repopulating the ν_e and the $\bar{\nu}_e$ sectors and, as a consequence, Y_e does not decrease further as happens in the case at $t_0 = 2.9$ s. Comparing the Y_e profiles in the matter + ν background and matter background cases, we find that $Y_e(\text{matter} + \nu) - Y_e(\text{matter}) \simeq 0.02$. For both the discussed profiles, ν–ν interactions are triggered at smaller radii than usually expected in the active case by the presence of non-zero off-diagonal terms in the density matrices of neutrinos and antineutrinos, similar to what was discussed in Dasgupta et al. (2010) for three active flavors. The role played by the neutrino self-interactions becomes particularly evident at late postbounce times t_0, because the matter background is lower and, therefore, the effective mixing angle θ_{13} (Duan et al. 2008; Esteban-Pretel et al. 2008) is larger than in the early cooling phase.

REFERENCES

Abazajian, K. N., Acero, M. A., Agarwalla, S. K., et al. 2012, arXiv:1204.5379
Aguilar, A., Auerbach, L. B., Burman, R. L., et al. 2001, PhRvD, 64, 112007
Aguilar-Arevalo, A. A., Anderson, C. E., Brice, S. J., et al. 2009a, PhRvL, 103, 111801
Aguilar-Arevalo, A. A., Anderson, C. E., Bazarko, A. O., et al. 2009b, PhRvL, 102, 101802
Archidiacono, M., Fornengo, N., Gariazzo, S., Giunti, C., Hannestad, S., & Laveder, M. 2014, JCAP, 6, 31
Archidiacono, M., Fornengo, N., Giunti, C., Hannestad, S., & Melchiorri, A. 2013, PhRvD, 87, 125034
Arcones, A., & Montes, F. 2011, ApJ, 731, 5
Arcones, A., & Thielemann, F.-K. 2013, JPhG, 40, 013201
Arnould, M., Goriely, S., & Takahashi, K. 2007, PhR, 450, 97
Beun, J., McLaughlin, G. C., Surman, R., & Hix, W. R. 2006, PhRvD, 73, 093007

Bruenn, S. W. 1985, ApJS, 58, 771
Capozzi, F., Fogli, G. L., Lisi, E., et al. 2014, PhRvD, 89, 093018
Chakraborty, S., Fischer, T., Mirizzi, A., Saviano, N., & Tomas, R. 2011, PhRvD, 84, 025002
Dasgupta, B., & Dighe, A. 2008, PhRvD, 77, 113002
Dasgupta, B., Mirizzi, A., Tamborra, I., & Tomàs, R. 2010, PhRvD, 81, 093008
Dasgupta, B., Raffelt, G. G., & Tamborra, I. 2010, PhRvD, 81, 073004
Donini, A., Hernández, P., López-Pavón, J., Maltoni, M., & Schwetz, T. 2012, JHEP, 7, 161
Duan, H., Friedland, A., McLaughlin, G. C., & Surman, R. 2011a, JPhG, 38, 035201
Duan, H., Friedland, A., McLaughlin, G. C., & Surman, R. 2011b, JPhG, 38, 035201
Duan, H., Fuller, G. M., Carlson, J., & Qian, Y.-Z. 2006, PhRvD, 74, 105014
Duan, H., Fuller, G. M., & Qian, Y.-Z. 2008, PhRvD, 77, 085016
Duan, H., Fuller, G. M., & Qian, Y.-Z. 2010, ARNPS, 60, 569
Esteban-Pretel, A., Mirizzi, A., Pastor, S., et al. 2008, PhRvD, 78, 085012
Esteban-Pretel, A., Pastor, S., Tomás, R., Raffelt, G. G., & Sigl, G. 2007, PhRvD, 76, 125018
Fetter, J., McLaughlin, G. C., Balantekin, A. B., & Fuller, G. M. 2003, APh, 18, 433
Fetter, J. M. 2000, PhD thesis, Univ. Wisconsin-Madison
Fischer, T., Martínez-Pinedo, G., Hempel, M., & Liebendörfer, M. 2012, PhRvD, 85, 083003
Fischer, T., Whitehouse, S. C., Mezzacappa, A., Thielemann, F.-K., & Liebendörfer, M. 2010, A&A, 517, A80
Fogli, G., Lisi, E., Marrone, A., & Mirizzi, A. 2007, JCAP, 12, 10
Fogli, G., Lisi, E., Marrone, A., & Tamborra, I. 2009a, JCAP, 4, 30
Fogli, G., Lisi, E., Marrone, A., & Tamborra, I. 2009b, JCAP, 10, 2
Fogli, G. L., Lisi, E., Marrone, A., Mirizzi, A., & Tamborra, I. 2008, PhRvD, 78, 097301
Fogli, G. L., Lisi, E., Marrone, A., & Palazzo, A. 2006, PrPNP, 57, 742
Fröhlich, C., Martínez-Pinedo, G., Liebendörfer, M., et al. 2006a, PhRvL, 96, 142502
Fröhlich, C., Hauser, P., Liebendörfer, M., et al. 2006b, ApJ, 637, 415
Fuller, G. M., & Meyer, B. S. 1995, ApJ, 453, 792
Giunti, C., & Laveder, M. 2011a, PhLB, 706, 200
Giunti, C., & Laveder, M. 2011b, PhRvD, 84, 093006
Giunti, C., Laveder, M., Li, Y. F., Liu, Q. Y., & Long, H. W. 2012, PhRvD, 86, 113014
Giunti, C., Laveder, M., Li, Y. F., & Long, H. W. 2013, PhRvD, 88, 073008
Giusarma, E., Di Valentino, E., Lattanzi, M., Melchiorri, A., & Mena, O. 2014, PhRvD, 90, 043507
Gonzalez-Garcia, M. C., & Maltoni, M. 2008, PhR, 460, 1
Hamann, J., Hannestad, S., Raffelt, G. G., Tamborra, I., & Wong, Y. Y. Y. 2010, PhRvL, 105, 181301
Hannestad, S., Raffelt, G. G., Sigl, G., & Wong, Y. Y. Y. 2006, PhRvD, 74, 105010
Hidaka, J., & Fuller, G. M. 2007, PhRvD, 76, 083516
Hillebrandt, W., Nomoto, K., & Wolff, R. G. 1984, A&A, 133, 175
Hinshaw, G., Larson, D., Komatsu, E., et al. 2013, ApJS, 208, 19
Hoffman, R. D., Müller, B., & Janka, H.-T. 2008, ApJL, 676, L127
Hoffman, R. D., Woosley, S. E., & Qian, Y.-Z. 1997, ApJ, 482, 951
Horowitz, C. J., & Li, G. 1999, PhRvL, 82, 5198
Hou, Z., Keisler, R., Knox, L., Millea, M., & Reichardt, C. 2013, PhRvD, 87, 083008
Hüdepohl, L., Müller, B., Janka, H.-T., Marek, A., & Raffelt, G. G. 2010, PhRvL, 104, 251101
Ishimaru, Y., & Wanajo, S. 1999, ApJL, 511, L33
Janka, H.-T. 2012, ARNPS, 62, 407
Janka, H.-T., Müller, B., Kitaura, F. S., & Buras, R. 2008, A&A, 485, 199
Karagiorgi, G., Djurcic, Z., Conrad, J. M., Shaevitz, M. H., & Sorel, M. 2009, PhRvD, 80, 073001
Keil, M. T., Raffelt, G. G., & Janka, H.-T. 2003, ApJ, 590, 971
Keränen, P., Maalampi, J., Myyryläinen, M., & Riittinen, J. 2007, PhRvD, 76, 125026
Kitaura, F. S., Janka, H.-T., & Hillebrandt, W. 2006, A&A, 450, 345
Kopp, J., Machado, P. A. N., Maltoni, M., & Schwetz, T. 2013, JHEP, 5, 50
Kopp, J., Maltoni, M., & Schwetz, T. 2011, PhRvL, 107, 091801
Lodders, K. 2003, ApJ, 591, 1220
Martínez-Pinedo, G., Fischer, T., Lohs, A., & Huther, L. 2012, PhRvL, 109, 251104
Martínez-Pinedo, G., Ziebarth, B., Fischer, T., & Langanke, K. 2011, EPJA, 47, 98
McLaughlin, G. C., Fetter, J. M., Balantekin, A. B., & Fuller, G. M. 1999, PhRvC, 59, 2873
McLaughlin, G. C., Fuller, G. M., & Wilson, J. R. 1996, ApJ, 472, 440
Mention, G., Fechner, M., Lasserre, T., et al. 2011, PhRvD, 83, 073006
Meyer, B. S., Mathews, G. J., Howard, W. M., Woosley, S. E., & Hoffman, R. D. 1992, ApJ, 399, 656
Meyer, B. S., McLaughlin, G. C., & Fuller, G. M. 1998, PhRvC, 58, 3696
Mikheyev, S. P., & Smirnov, A. Y. 1985, YaFiz, 42, 1441
MiniBooNE Collaboration, Aguilar-Arevalo, A. A., Brown, B. C., et al. 2013, PhRvL, 110, 161801
Ning, H., Qian, Y.-Z., & Meyer, B. S. 2007, ApJL, 667, L159
Nomoto, K. 1987, ApJ, 322, 206
Nunokawa, H., Peltoniemi, J. T., Rossi, A., & Valle, J. W. F. 1997, PhRvD, 56, 1704
Otsuki, K., Tagoshi, H., Kajino, T., & Wanajo, S.-Y. 2000, ApJ, 533, 424
Palazzo, A. 2013, MPLA, 28, 30004
Planck Collaboration, Ade, P. A. R., Aghanim, N., et al. 2014, A&A, 571, A16
Poelarends, A. J. T., Herwig, F., Langer, N., & Heger, A. 2008, ApJ, 675, 614
Pruet, J., Hoffman, R. D., Woosley, S. E., Janka, H.-T., & Buras, R. 2006, ApJ, 644, 1028
Qian, Y.-Z., & Fuller, G. M. 1995, PhRvD, 52, 656
Qian, Y.-Z., & Woosley, S. E. 1996, ApJ, 471, 331
Reddy, S., Prakash, M., & Lattimer, J. M. 1998, PhRvD, 58, 013009
Reid, B. A., Verde, L., Jimenez, R., & Mena, O. 2010, JCAP, 1, 3
Roberts, L. F. 2012, ApJ, 755, 126
Roberts, L. F., Reddy, S., & Shen, G. 2012, PhRvC, 86, 065803
Sarikas, S., Raffelt, G. G., Hüdepohl, L., & Janka, H.-T. 2012, PhRvL, 108, 061101
Shen, H., Toki, H., Oyamatsu, K., & Sumiyoshi, K. 1998, NuPhA, 637, 435
Sigl, G., & Raffelt, G. 1993, NuPhB, 406, 423
Strumia, A. 2002, PhLB, 539, 91
Takahashi, K., Witti, J., & Janka, H.-T. 1994, A&A, 286, 857
Tamborra, I., Müller, B., Hüdepohl, L., Janka, H.-T., & Raffelt, G. 2012a, PhRvD, 86, 125031
Tamborra, I., Raffelt, G. G., Hüdepohl, L., & Janka, H.-T. 2012b, JCAP, 1, 13
Thielemann, F.-K., Arcones, A., Käppeli, R., et al. 2011, PrPNP, 66, 346
Thompson, T. A., Burrows, A., & Meyer, B. S. 2001, ApJ, 562, 887
Wanajo, S. 2006, ApJ, 647, 1323
Wanajo, S., & Ishimaru, Y. 2006, NuPhA, 777, 676
Wanajo, S., Janka, H.-T., & Kubono, S. 2011a, ApJ, 729, 46
Wanajo, S., Janka, H.-T., & Müller, B. 2011b, ApJL, 726, L15
Wanajo, S., Janka, H.-T., & Müller, B. 2013a, ApJL, 767, L26
Wanajo, S., Janka, H.-T., & Müller, B. 2013b, ApJL, 774, L6
Wanajo, S., Kajino, T., Mathews, G. J., & Otsuki, K. 2001, ApJ, 554, 578
Wanajo, S., Nomoto, K., Janka, H.-T., Kitaura, F. S., & Müller, B. 2009, ApJ, 695, 208
Wanajo, S., Tamamura, M., Itoh, N., et al. 2003, ApJ, 593, 968
Wolfenstein, L. 1978, PhRvD, 17, 2369
Woosley, S. E., Heger, A., & Weaver, T. A. 2002, RvMP, 74, 1015
Woosley, S. E., Wilson, J. R., Mathews, G. J., Hoffman, R. D., & Meyer, B. S. 1994, ApJ, 433, 229
Wu, M.-R., Fischer, T., Huther, L., Martínez-Pinedo, G., & Qian, Y.-Z. 2014, PhRvD, 89, 061303
Wu, M.-R., Qian, Y.-Z., Martínez-Pinedo, G., Fischer, T., & Huther, L. 2015, PhRvD, 91, 065016